A 200-MHZ FULLY-DIFFERENTIAL CMOS FRONT-END WITH AN

ON-CHIP INDUCTOR FOR MAGNETIC RESONANCE IMAGING

A Thesis

by

JULIO ENRIQUE AYALA II

Submitted to the Office of Graduate Studies of
Texas A&M University
in partial fulfillment of the requirements for the degree of

MASTER OF SCIENCE

December 2005

Major Subject: Electrical Engineering

A 200-MHZ FULLY-DIFFERENTIAL CMOS FRONT-END WITH AN

ON-CHIP INDUCTOR FOR MAGNETIC RESONANCE IMAGING

A Thesis

by

JULIO ENRIQUE AYALA II

Approved by:

Co-Chairs of Committee,	Takis Zourntos
	Steven Wright
Committee Members,	Jose Silva-Martinez
	Karen Butler-Purry
	Francis Narcowich
Head of Department,	Costas Georghiades

December 2005

Major Subject: Electrical Engineering

ABSTRACT

A 200-MHz Fully-Differential CMOS Front-End with an

On-Chip Inductor for Magnetic Resonance Imaging. (December 2005)

Julio Enrique Ayala II, B.S., Texas A&M University

Co–Chairs of Advisory Committee: Dr. Takis Zourntos
Dr. Steven Wright

Recently, there is a growing interest in applying electronic circuit design for biomedical applications, especially in the area of nuclear magnetic resonance (NMR). NMR has been used for many years as a spectroscopy technique for analytical chemistry. Previous studies have demonstrated the design and fabrication of planar spiral inductors (microcoils) that serve as detectors for nuclear magnetic resonance microspectroscopy.

The goal of this research was to analyze, design, and test a prototype integrated sensor, which consisted of a similar microcoil detector with analog components to form a multiple-channel front-end for a magnetic resonance imaging (MRI) system to perform microspectroscopy. The research has succeeded in producing good functionality for a multiple-channel sensor. The sensor met expectations compared to similar one-channel systems through experiments in channel separation and good signal-to-noise ratios.

To God

ACKNOWLEDGMENTS

The quest for knowledge is a journey that is long and difficult but equally rewarding. It is a journey not many people would endeavor for fear of failure. That is why it is a necessity to have strong support from the people around you to make this journey a success. Without the support from many people, I would not have completed my graduate work.

First and foremost, I thank my Lord and Saviour Jesus Christ. Through faith in Him, all things are possible especially during the times I doubted my abilities to complete my education. Through His blessings, He has carried me through the good and difficult times.

I thank my graduate advisor, Dr. Takis Zourntos, for the constant guidance and support these past two years. It is through your trust in my knowledge and abilities that we were able to explore great research. Also, I thank Dr. Steven Wright for the time you took to help with my research in magnetic resonance imaging and for allowing me to use your testing facilities.

I thank all the members of my committee: Dr. Jose Silva-Martinez, Dr. Karen Butler-Purry, and Dr. Francis Narcowich. I appreciate the time you took to support my thesis. Special thanks go to Dr. Fred Strieter for the opportunity to work for you as a grader and teaching assistant. Many times you have taken time out of your day to become a mentor and friend. I thank every professor and staff member in the Analog & Mixed Signal Center and Electrical Engineering Department who has helped and supported me throughout the years, especially Dr. Edgar Sanchez-Sinencio and Ella Gallagher.

Throughout my Master's education, I have developed great friendships that helped me endure this long journey. I thank Jon and Kat Gardiol, Justin War-

ren, and Adam Vance. It was a great experience living with each one of you and I thank you for making me a part of your family. Special thanks go to Abraham Islas and Rob Milliken who have been great colleagues as well as great friends. I thank every student in the Analog & Mixed Signal Center especially Artur Lewinski, Sathya Venkatesh, and Rida Assaad.

Without the love and support from Sarah Diaz, my education would have been impossible. Your patience and faith in me carried me through my education especially during the most difficult of times. The love and prayers from your family is truly cherished.

Lastly, I thank my entire family for the never-ending love and faith that was given to me. I thank my brother, Aurelio, for being the person I look up to and making sure that I stay on task. I thank my parents for basically everything in my short life. You brought me into this world with dreams and aspirations. Without your support and confidence, I could not have achieved my own dreams and aspirations. Thank you for raising me the correct way.

TABLE OF CONTENTS

LIST OF TABLES

LIST OF FIGURES

CHAPTER I

INTRODUCTION

Nuclear magnetic resonance is a phenomenon which occurs when the nuclei of certain atoms are immersed in a static magnetic field and are exposed to a second oscillating magnetic field of the correct frequency. Some nuclei experience this phenomenon, and others do not, depending upon whether they possess a property called spin. Most matter that is examined with NMR is composed of molecules made up of atoms. The majority of living tissue is comprised of water molecules, where a water molecule has one oxygen and two hydrogen atoms. Looking past the electron cloud of a hydrogen atom, there is a nucleus composed of a single proton. This hydrogen proton possesses the spin property, which can be thought of as a small magnetic field, and will cause the nucleus to produce an NMR signal inside a static magnetic field. Since not all nuclei possess the spin property, it makes the hydrogen in living tissue ideal for NMR [1].

When the static magnetic field is applied to a hydrogen atom, the proton nucleus tends to align either parallel or anti-parallel to the static field, B_0. The spin causes the nuclear magnet to precess about the applied magnetic field at a constant angle. The spin frequency is dictated by the Lamor relationship as seen in (1.1). According to this equation, the precessing frequency is proportional to the magnetic field strength. The constant γ is specific to each nuclei and, in the case for NMR, the nuclei is Hydrogen.

$$f = \gamma \cdot B_0 \quad [\text{Hz}] \qquad (1.1)$$

$$\gamma = 42.577 \cdot 10^6 \quad [s^{-1} \cdot T^{-1}] \qquad (1.2)$$

This thesis follows the style and format of *IEEE Journal of Solid-State Circuits.*

As shown in Figure 1, both B_0 and M_0 are aligned during equilibrium so that no force is created between them and, hence, no signal would be generated. Therefore, the net magnetization vector M_0 must be tipped away from the Z-axis.
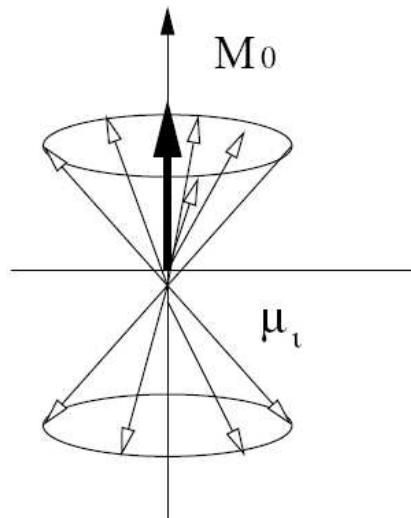
Fig. 1. Net Magnetization Vector

The net magnetization is moved from the equilibrium position by using a RF transmitter pulse, which has a secondary and oscillating magnetic field associated with it, referred to as B_1. The bulk magnetization moves away from its equilibrium position when the oscillation reaches near the Larmor frequency. This disturbed magnetization then starts precessing about the transverse plane at the Lamor frequency. This motion can be detected as a voltage by the receiver coils [2].

Spectroscopy is the study of the interaction of electromagnetic radiation with matter. Nuclear magnetic resonance spectroscopy is the use of the NMR phenomenon to study physical, chemical, and biological properties of matter. As a result, NMR spectroscopy finds applications in several areas of science. NMR spectroscopy is routinely used by chemists to study chemical structure using simple one-dimensional

techniques. A two-dimensional approach is used to determine structures of more complicated molecules. These techniques are replacing x-ray crystallography for the determination of protein structure. Time domain NMR spectroscopic techniques are used to probe molecular dynamics in solutions. Solid state NMR spectroscopy is used to determine the molecular structure of solids [1].

Magnetic resonance imaging is a technique used primarily in medical settings to produce high quality images of the inside of the human body. It provides a "window" into the body that had not previously been available by actually interrogating the nuclear environment of selected nuclei [3]. MRI is based on the basic principles of nuclear magnetic resonance.

A. Applications

Electronics has been instrumental in processing the NMR signals in the mentioned biomedical applications. Without the use of electronics, it would prove to be difficult to interpret and analyze the NMR signals detected from different living tissues. Researchers are continually trying to expand the applications of nuclear magnetic resonance. With over 10,000 clinical magnetic resonance systems in use, new technologies have helped to provide new ideas in this field. Using microelectronic circuit design for magnetic resonance systems creates a new method for these types of systems at a smaller and, possibly, a more efficient scale. Currently, microelectronic design is making strides in the areas of real-time imaging and molecular spectroscopy [2].

1. Real-Time Imaging

The Magnetic Resonance Systems Lab (MRSL) at Texas A&M University has currently the fastest real-time MRI systems. The MRI system designed by MRSL uses

a 64 element planar array and a custom built 64 channel receiver system that can construct a 64 x 256 resolution image, demonstrating the ability to form complete images from a single echo acquisition. Single echo acquisition (SEA) imaging enables the acquisition of an entire image in a single echo using an array of coils. With the receiver and the array, it is capable of generating complete images during successive echo acquisitions, potentially enabling extremely rapid frame rates. The MRSL has experimented using single echo acquisition imaging to take magnetic resonance movies at frame rates of 125 frames per second. This speed is limited by the minimum practical repetition time of the lab's GE Omega, approximately 8 milliseconds. On modern clinical systems sustained frame rates of 500 to 1000 frames per second should be possible [4]. Possible applications for real-time imaging include detection of cardiac arrhythmia, functional/dynamic maps of brain activity, etc., which will be done without risk to the patient.

2.   Molecular Spectroscopy

Since sensitivity of NMR radio frequency (RF) coils has been an important issue, many researchers have worked on the miniaturization of RF detection devices for molecular spectroscopy. Possible applications for molecular spectroscopy include early cancer detection and pharmaceutical synthesis. There have been two approaches that have been recently researched on these types of devices.

1. The use of solenoidal microcoils as flow probes for static and dynamic NMR measurements.

2. The use of planar microcoils in a microelectronic fabrication technology.

Most solenoidal microcoils are made using a long capillary to be filled with an observed liquid sample. In [5], an implantable solenoidal microcoil is designed to be

used in NMR microspectroscopy experiments in a 2-Tesla magnet (85.13-MHz). The outer diameter of the coil was approximately 200 μm and the length was 580 μm. The coil was able to produce proton spectra of deionized water and butter. The spectra demonstrated good signal-to-noise.

Planar microcoils are researched because the fabrication process guarantees a good reproducibility. In addition, RF coils can be reduced in size and be integrated with electronic circuits. Depending on their structures, they could be used as implantable devices for selective detection of living metabolites in tissues [5]. In [6], the use of planar microcoils was demonstrated in high-resolution NMR microspectroscopy. Liquid samples were loaded into a fused silica capillary positioned 50 μm above a 3.5-turn microcoil so that approximately 1 nL of the sample was present above the sensitive region of the microcoil. At 5.9-Tesla magnet (250-MHz), NMR microspectroscopy was performed with good signal-to-noise results of the water.

B.   Radio Frequency Technology

To gain a general, preliminary view of NMR applications and the thesis research, a brief background of the RF technology will be discussed. It is necessary to know some background in RF technology because the MRI system is based on the simple analog architecture of a wireless RF receiver, as shown in Figure 2.
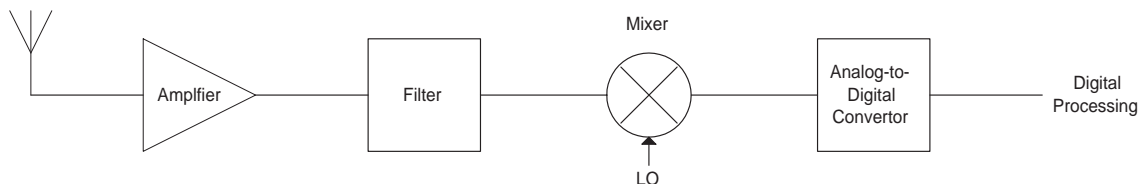
Fig. 2. Generic RF Receiver System

In the receive path, the signal is amplified, filtered, downconverted by the mixer, and digitized for digital processing. Subsequently, demodulation, equalization, decoding and deinterleaving, and decompression are performed in the digital domain. In most cases, the digital data would then be converted to analog form by a digital-to-analog converter, amplified, and applied to a speaker [7].

This generic type of RF receiver system is the basis of many wireless products such as cellular phones, wireless local area networks, global positioning systems, RF identification systems, and home satellite networks. Although each product provides different complexities and challenges in terms of circuit design, these systems proved to have great potential for rapid growth.

The IC technology for RF circuits consistently continues to change. Performance, cost, and time to market are factors that influence the choice of technologies in the RF industry. In addition, issues such as level of integration, form factor, and prior experience play important roles for designers [7]. There are three contending technologies that constitute the major section of the RF market. While GaAs and silicon bipolar and BiCMOS technologies have been the most popular and successful, CMOS technologies have become an increased contender in the RF market.

C. Motivation

An increased demand for research in the field of nuclear magnetic resonance has provided opportunities to use microelectronic design for two new applications on which this research will focus. Real-time imaging at a small scale will require a multi-chip module comprised of a receiver microcoil, preamp, analog multiplexing, filtering, and high resolution A/D converter. Molecular spectroscopy for chemical composition will require a similar module as real-time imaging, but with the addition of three-

dimensional MEMS-based coils for enhanced sensitivity of small-scale samples.

The basic architecture for these two applications for a single-channel receiver is shown in Figure 3; this can be referred to as a digital coil. It is possible to add a mixing component to downconvert the high-frequency magnetic resonance signal, which can be placed before the A/D converter.
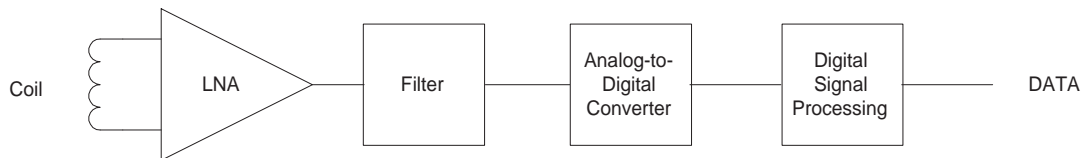
Fig. 3. Single Digital Coil Channel

Real-time imaging requires the use of an array of these digital coils multiplexed to analyze single channels of different parts of the object being imaged. A system diagram of an array-based NMR chip for real-time imaging is shown in Figure 4.

This research is currently being carried out in collaboration with the Magnetic Resonance Systems Lab at Texas A&M University. MRSL has a strong interest in the process of putting a MRI receiver on an integrated circuit. The limitation of the MRSL real-time MRI system is integration and packaging. The size of the sensors is an issue since an array of more than 64 planar coils will not fit inside the system, and we suspect that greater sensitivity can be realized with integrated electronics. MRSL has provided the use of their MRI system for testing purposes for this type of research.

The purpose of this research is to design a multi-channel MRI front-end system for microspectroscopy on an integrated circuit. The system will be mounted onto a PCB board to process all channels for good functionality.
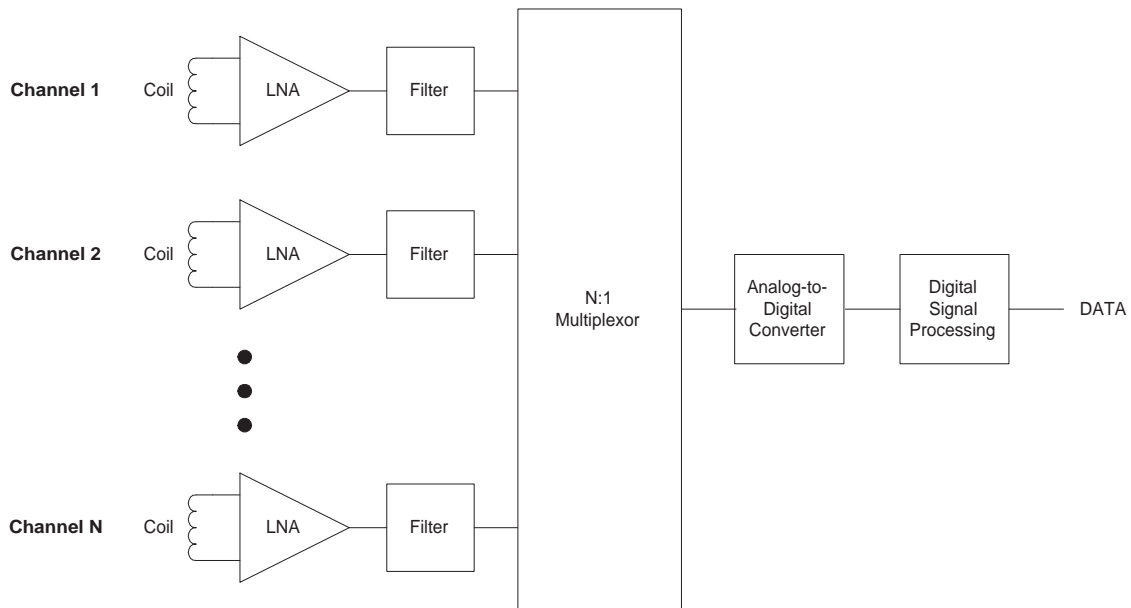
Fig. 4. Array Based NMR Chip

D. Project Description

The proposed integrated circuit was designed to operate in a MRI system operating in a 4.7-Tesla magnetic field at a 200-MHz resonant frequency. A single-channel MRI front-end system is shown in Figure 5, which will consist of a microcoil, variable capacitor, preamplifier, and bandpass filter. The integrated circuit designed will consist of two channels with all parts shown in Figure 5 excluding the bandpass filter.

- The microcoil block will serve as the detector for the MRI system. During the magnetization of the system, an RF pulse will be applied to induce a small voltage across the microcoil that will be needed to process the image. For each channel of the system, the microcoil will be designed as a planar rectangular-shaped spiral inductor using METAL4 in the TSMC 0.35-μm CMOS Technology.

- The variable capacitor (varactor) in parallel with the microcoil is required to keep the signal at its resonant frequency of 200-MHz. The varactor will be a
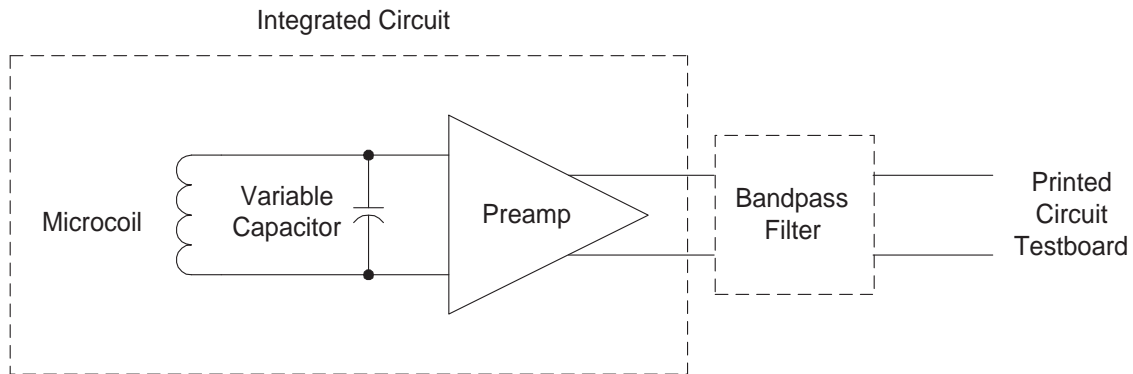
Fig. 5. Single-Channel MRI Front-End System

MOS transistor-based design.

- The preamplifier block will boost the voltage detected on the microcoil approximately 40 dB while minimizing the noise from active devices. This block will essentially consist of multiple stages of basic differential pairs with large currents to maximize gain. Each stage will be equal in terms of low gain and bandwidth. The purpose of the low gain is to minimize noise by keeping the drain resistances of the differential pair low, therefore, keeping thermal noise low.

- The bandpass filter block will suppress unwanted frequencies around the resonant frequency of 200-MHz. The filter will have a 0-dB gain in the passband (197.5-202.5-MHz) and have at least a 30-dB attenuation in the stopband (170-MHz and 230-MHz).

E.   Integrated Circuit Design Planning

The planning for the design and fabrication of the MRI system is essential for a successful design. Different design tools was used for each block of the MRI front-end system, while careful layout and fabrication planning was used to ensure a good

design. Test characterization of the MRI system is vital to this research. It is important to demonstrate that the integrated circuit receives and amplifies a signal while suppressing the noise from other frequencies.

1.   Simulation

A computer tool named ASITIC (Analysis and Simulation of Inductors and Transformers in Integrated Circuits) was used to design and model the microcoil for highest quality factor, reasonable size, and inductance according to the CMOS technology. All other blocks were simulated using macromodels in the Cadence to verify functionality. The blocks were then simulated at transistor level in SpectreS using the TSMC 0.35-μm CMOS SPICE model parameters in Cadence. Monte Carlo simulations were performed to ensure that the design will be robust during manufacturing process variations.

2.   Layout

Layout was done using Virtuoso in Cadence for all blocks in the MRI system. Good techniques and matching were used, and metal density requirements as stated by MOSIS were considered.

3.   Project Size

The layout of the integrated circuit occupies 4 mm by 4 mm. The circuit contains two large inductors that occupy most of the chip area. The MOS transistors are large to accommodate large currents for the preamplifier block.

4. Packaging Requirements

The integrated circuit contains 44 functional bondpads. It has been determined by testing in a 4.7-Teslas magnet that the ceramic packaging provided by MOSIS will be ferrous and the functionality of the system will not be good. Therefore, it was recommended the integrated circuit needs to be unpackaged (loose die) when used inside the MRI system. Also, some of the dies were packaged in a QFP44 plastic package for test characterization outside the MRI system.

5. Circuit Fabrication

The integrated circuit was fabricated courtesy of the MOSIS Educational Research Program using the TSMC 0.35-μm CMOS Technology.

6. Test Characterization

The MRI front-end system operates with a 3.3-Volt power supply. Test measurements were carried out using the Biomedical Imaging Group and Analog & Mixed Signal Center's measurement equipment, such as the digital power supply, the spectrum analyzer, the mixed signal oscilloscope, and the digital multimeter. Other components needed to be constructed for testing of the system, such as a RF transmitter.

It was planned to have two major components of the testing phase for this integrated circuit. First, the packaged integrated circuit was characterized and tested outside of the MRI system core. Second, it was planned to have the unpackaged die mounted onto the printed circuit testboard by a third-party vendor for insertion into the MRI system core. This would test a small-scale fluid sample inside the core for spectroscopy. Financially, it was not possible to perform this test, but it needs to be an essential test for the next version of the MRI system prototype.

F.   Challenges and Requirements

There are a few challenges to the design of the MRI front-end system. First, the microcoil block needed to have a moderate quality factor to ensure a good response on the detected signal. It is difficult to accurately design an inductor using CMOS technology due to the lossy Silicon substrate. With a quality design of the inductor, the overall performance of the system can increase. Despite the design difficulty, the low cost of Silicon circuit fabrication and the potential for integration with baseband circuits makes Silicon a popular process choice. Also, the preamplifier block has low noise requirements, which proved to be a challenge.

The major requirement of the MRI front-end system is the experimental test phase. It was required to have comparable signal-to-noise results than that seen in previous research studies. Since, the integrated circuit is a multiple-channel system, it is required to have some degree of separation between the two channels in terms of interference.

G.   Thesis Outline

The following chapters will discuss the design of each fundamental block of the MRI system. Chapter II will discuss the background information and design of the planar microcoil of the system. Chapter III will discuss the design of the preamplifier block of the system. Chapter IV will discuss the bandpass filter block of the system with a preliminary system level design. Chapter V will analyze the system level simulations and layout considerations; it will also discuss the experimental analysis of the MRI system. Chapter VI concludes the project with system analysis as well as future work planned for the system.

CHAPTER II

MICROCOIL INDUCTOR

The microcoil inductor serves as the detector of the MRI front-end system. During the magnetization of the system, a 200-MHz RF pulse will be applied to induce a small voltage across the microcoil needed to process an image. This chapter discusses the background of the microcoil circuit in this type of system and the tools used to design this block.

A.   Microcoil Background

The signal produced in a magnetic resonance receive coil is a time-varying signal at radio frequency centered at the Larmor frequency, which is given by (2.1) [3].

$$f \;=\; \gamma \cdot B_0 \quad [\text{Hz}] \tag{2.1}$$

$$\gamma \;=\; 42.577 \cdot 10^6 \quad [s^{-1} \cdot T^{-1}] \tag{2.2}$$

Each RF pulse produces a sinusoidal signal at a frequency dependent on the magnetic field inside of the MRI system. For this research, the magnetic field is $B_0 = 4.7$ T, and following (2.1), this will result in a sinusoidal signal at 200-MHz.

A microcoil inductor will have intrinsic capacitance and resistance in addition to the inductance. However, the intrinsic capacitance of the inductor can be neglected if the inductor is used at a frequency much less than the self-resonant frequency. For the microcoil in this research, the self-resonant frequency is in the gigahertz range and, therefore, the intrinsic capacitance will be neglected. As a result, a realistic inductor can be represented as an inductance, L, in series with an intrinsic resistance, R, driven by the sinusoidal signal across the circuit [8].

Since magnetic resonance occurs at a fixed frequency for a specific magnetic field, the microcoil circuit needs to operate efficiently at this frequency. A possible approach is to tune the circuit with a capacitive-reactive element to provide appropriate impedance at the desired frequency. This can be done by placing a capacitor in parallel with the microcoil, as shown in Figure 6.
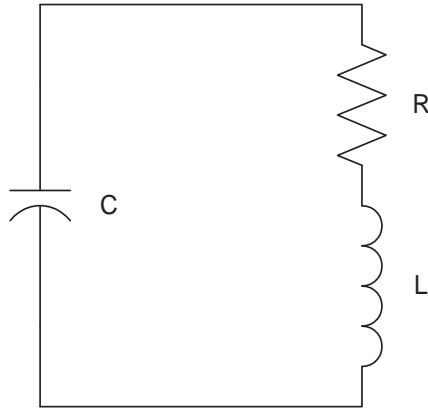
Fig. 6. Parallel-Tuned Microcoil Circuit

The microcoil becomes resonant when the impedance is purely resistive and the inductive and capacitive impedance have equal magnitude, seen in (2.3).

$$\omega \cdot L = \frac{1}{\omega \cdot C} \tag{2.3}$$

Therefore, the resonant frequency, f_o, becomes (2.4).

$$f_o = \frac{1}{2 \cdot \pi \cdot \sqrt{L \cdot C}} \quad [\text{Hz}] \tag{2.4}$$

At the resonant frequency, the circuit impedance is minimum and equal to the resistance of the circuit, R. An important factor of the microcoil circuit is given by quality factor, Q. Quality factor determines the sharpness of the circuit's response, thus, a high quality factor is ideal to achieve the best response of the system. For

this microcoil circuit, the quality factor at resonant frequency is (2.5).

$$Q = \frac{\omega_o \cdot L}{R} \qquad (2.5)$$

B. Inductor Model Analysis

Passive elements are integral building blocks in realizing fully integrated RF transceivers. The modeling of passive elements is essential to the design and optimization of these blocks, especially when the quality factor determines overall performance. Analysis of passive elements near silicon substrate requires solving of Maxwell's equations, which can be computationally expensive and time-consuming. Silicon integrated circuit spiral inductors and transformers are analyzed using electromagnetic analysis. With appropriate approximations, the calculations are reduced to electrostatic and magnetostatic calculations. ASITIC, Analysis and Simulation of Inductors and Transformers for Integrated Circuits, is a software tool that applies these approximations and calculations and aids the design and simulation of these passive elements [9, 10].

ASITIC is an interactive CAD tool that assists designers to analyze, model, and optimize passive and interconnect metal structures residing on a lossy conductive substrate, such as Silicon. This tool allows designers to plan and optimize the layout of a chip in the presence of magnetic and electrical interaction and coupling through the substrate and oxide layers of the integrated circuit. The analysis applied is used to design traditional square and polygon inductors and transformer structures, as well as multilayer metal structures and coupled inductors. ASITIC works with a mini-technology file (See Appendix A) that describes the substrate and metal layers of the technology process the design is using.

C. Inductor Fabrication and Specifications

A microcoil inductor can be built on a silicon substrate by using the multilevel inter-
connects that is provided with current silicon fabrication processes. A minimum of
two metal layers is needed to build a basic coil with an underpass contact to return
the inner terminal of the coil to the outside. The structure of an inductor is defined
by the number of turns (N), the metal width (W), the metal spacing (S), and the
total area covered (d_W by d_L), as shown in Figure 7.
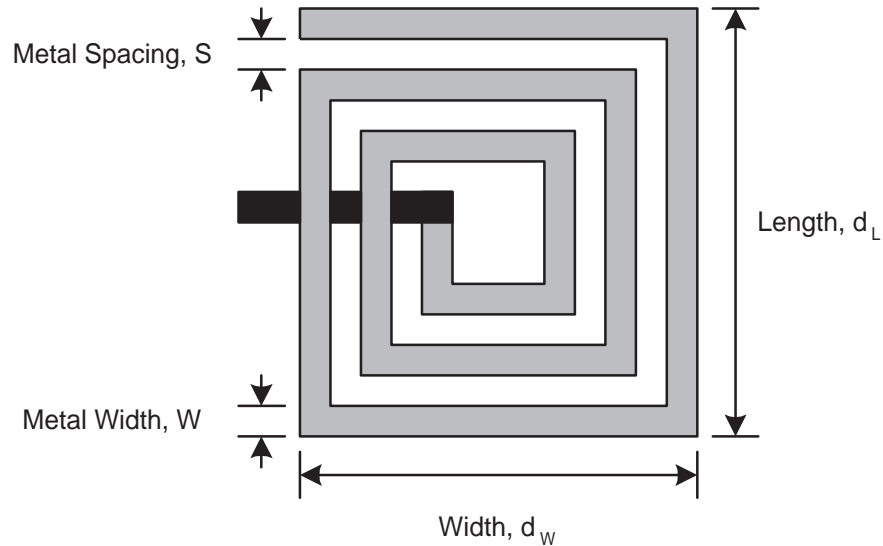
Fig. 7. Microcoil Inductor Fabrication Structure (N = 3 Turns)

The microcoil itself is modeled by an ideal inductance (L), a series resistance
(R) representing the ohmic losses in the coil, and the intrinsic capacitances. As
discussed earlier, the intrinsic capacitances may be neglected as long as the frequency
of operation is much less than the self-resonant frequency of the microcoil. Again,
the self-resonant frequency of the microcoil designed will be in the gigahertz range,
therefore, the intrinsic capacitances will be ignored.

Designing passive inductors in any fabrication technology can be very difficult. Changing the parameter structure, such as area, turns, metal spacing, and metal width can change the inductor characteristics. There are many tradeoffs to achieving certain characteristics for an inductor that will limit how it will be designed in a CMOS technology. Since inductors are fabricated using metal layers in any fabrication technology, the area consumed by the inductor will be a determining factor. An approach to increasing area is the choice of metal layer used. The thickest metal layer is desired to maximize the area of the inductor. Increasing area can also be done by increasing the length and width of an inductor or increasing the number of turns for a certain area. Changing the metal width and metal spacing can also affect the area of an inductor. The simple nature of an inductor is that when area is increased for an inductor, the inductance increases while the resistance decreases.

$$Area \uparrow \Rightarrow L \uparrow \Rightarrow R \downarrow$$

Based on (2.5), this kind of change will greatly affect the quality factor of the microcoil circuit. The rate of change of the inductance and resistance will not always be the same, therefore, there must be some tradeoff to getting the best quality factor based on the rate of change for different areas.

Although the microcoil design does not have any set value specifications, there is one determining characteristic in designing the microcoil. The major characteristic to designing the microcoil is achieving a moderately high quality factor. It is desired to achieve the best quality factor without sacrificing a large amount of area at a reasonable inductance and resistance.

D.   Microcoil Design

The ASITIC software tool assisted in designing the microcoil to achieve the best characteristics, especially quality factor. ASITIC contains a recursion tool to determine the highest quality factor for a set of parameters. The ASITIC design parameters used to determine the best microcoil are shown in Table I. In TSMC 0.35-μm CMOS Technology, METAL4 is the thickest metal that is ideal for inductor design. It is shown in the table that the maximum area of the inductor chosen is 2-mm by 2-mm. Large inductor sizes are not reasonable for integrated circuit fabrication because large area consumed in silicon is extremely expensive. The metal width and spacing range has enough variation to modify the area and change the characteristics of the inductor. The number of turns is randomly generated by ASITIC based on these design parameters.

Table I. ASITIC Design Parameters

Metal Layer	METAL4	
Inductor Width Range (μm)	500	2000
Metal Width Range (μm)	10	50
Metal Spacing Range (μm)	1	5
Inductance Range (nH)	1	200
Minimum Q	0.5	
Frequency (MHz)	200	

The recursion tool outputs possible microcoil and its respective characteristics into a text file. After using MATLAB to sort through the data, Table II shows prospective microcoils with the highest quality factors. The microcoil characteristics with the best quality factor are bolded in Table II.

Table II. Best Results for Microcoil Characteristics from ASITIC

Inductor Width (μm)	Metal Width (μm)	Metal Spacing (μm)	Turns	L (nH)	R (Ω)	Q
1500	30	1	10	121.5	30.98	2.884
1500	30	1	12	137.8	29.67	2.958
1500	30	1	14	148.1	27.42	2.973
1500	30	1	21	157.6	22.33	3.047
1500	30	2	7	118.6	30.91	3.402
1500	30	2	8	127.0	30.42	3.407
1500	**30**	**2**	**9**	**133.4**	**29.63**	**3.442**
1500	30	2	10	139.3	28.66	3.410
1500	30	2	11	143.5	27.63	3.349
1500	30	2	12	146.9	26.49	3.310
1500	30	2	13	149.0	25.58	3.270
1500	30	2	14	150.2	24.90	3.231
1500	30	2	15	151.4	24.08	3.169
1500	30	2	16	151.8	23.77	3.135
1500	30	2	17	153.1	22.87	3.089
1500	30	2	18	154.5	22.13	3.002
1500	30	2	19	155.8	21.45	2.985

Using the best microcoil characteristics and (2.4), the capacitor was calculated for the parallel-tuned microcoil circuit.

$$
\begin{aligned}
f_o &= 200 \quad \text{MHz} \\
R &= 29.63 \quad \Omega \\
L &= 133.4 \quad \text{nH} \\
C &= 4.73 \quad \text{pF}
\end{aligned}
$$

From (2.5), the quality factor was calculated, which is slightly different from the quality factor simulated in ASITIC.

$$Q = 5.658$$

The microcoil characteristics from ASITIC and hand-calculations can be verified with Cadence. Figure 8 shows the basic schematic to find the frequency response of the microcoil circuit. With the inductance and resistance values from ASITIC and the calculated parallel capacitance value, it is expected to see a response with a resonant frequency at 200-MHz with a Q of 5.658.
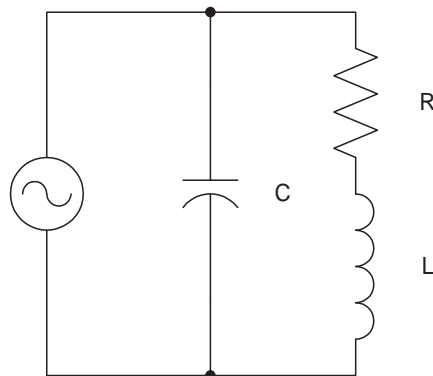
Fig. 8. Parallel-Tuned Microcoil Schematic for Frequency Response

Figure 9 shows the frequency response of the microcoil circuit. As expected, the resonant frequency and quality factor of the microcoil circuit are approximately equal to the specifications and hand-calculations.
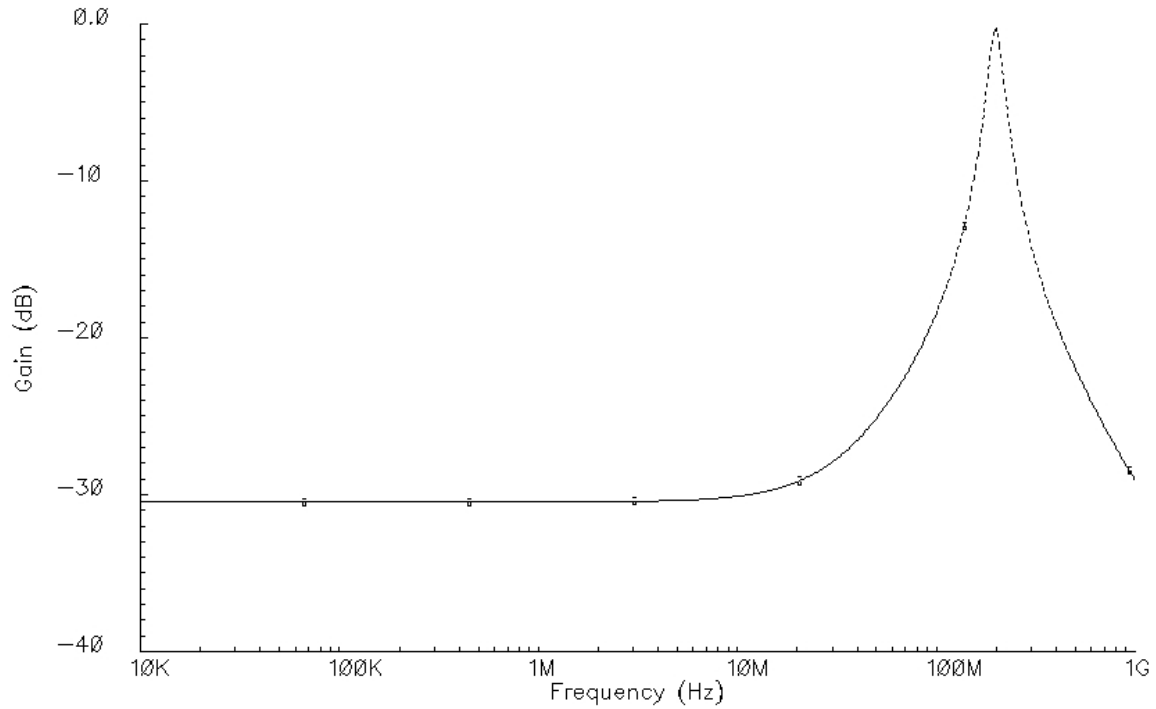
Fig. 9. Parallel-Tuned Microcoil Frequency Response

Table III shows the results for the frequency response of the microcoil circuit.

E.   Layout Considerations

The layout of the inductor is fairly simple when using ASITIC. Once the desired set of parameters has been found to achieve the specifications of the inductor, ASITIC draws the inductor using these parameters. The ASITIC drawing was then exported in a CIF file, which Cadence easily recognizes for layout purposes. A layer table is

Table III. Parallel-Tuned Microcoil Simulation Results

Resonant Gain	-0.3 dB
Resonant Frequency	199.5-MHz
Lower Cutoff Frequency	182.2-MHz
Upper Cutoff Frequency	217.5-MHz
Quality Factor	5.6516

needed to convert the layer mapping seen in ASITIC to the layer mapping Cadence can use to identify metal layers. Figure 10 shows the ASITIC inductor drawing and the Cadence inductor layout after being exported.

(a) ASITIC   (b) Cadence
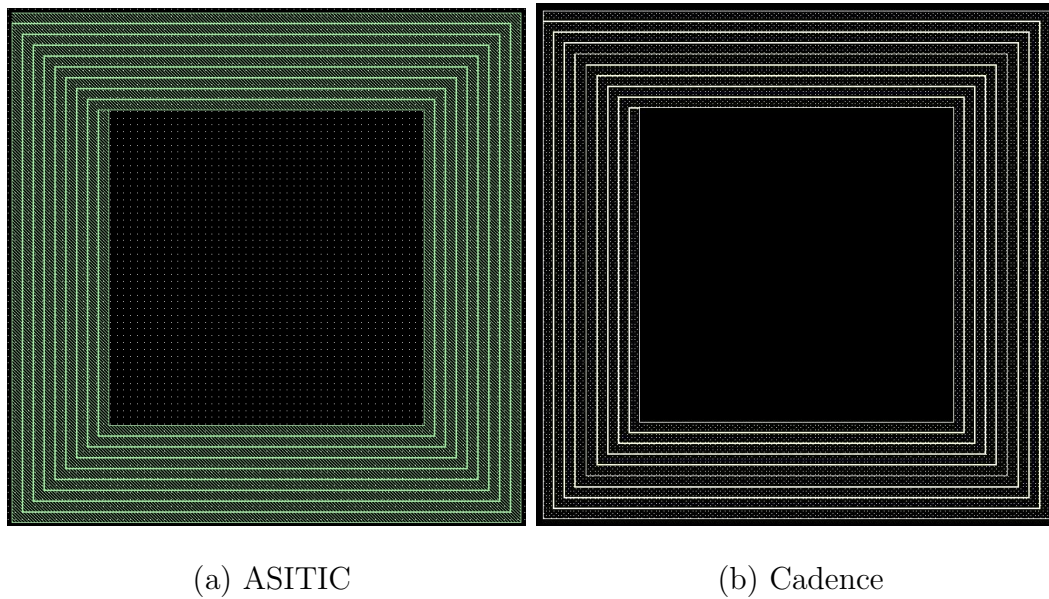
Fig. 10. Microcoil Spiral Inductor

F.   Other Microcoil Approaches

The lossy Silicon substrate and thin metal layers of CMOS/BiCMOS technology processes have contribute to the low quality factor (Q) of on-chip inductors. There have been approaches proposed to diminish the substrate loss and to increase Q, but these approaches required changes to the technology process. This type of change would increase cost and degrade active device performance. According to [11], the authors reported of enhancing Q of on-chip microcoils without any modification to CMOS/BiCMOS technology processes. The two most interesting approaches make use of two metal layers of a given technology.

1. Multilevel metal shunt has two metal layers in parallel to construct a spiral together.

2. Multilevel metal cascade has the top metal and bottom metal implemented as spirals individually and connected only at the center.

Other approaches are discussed but are not as effective of the multi-metal layer coils. In this report, the double metal shunt appears to be the most effective method to improve the Q of the spiral inductor. This approach will be implemented by a colleague in the next prototype of the MRI front-end system.

G.   Variable Capacitor

A varactor diode or tuning diode is a type of diode used in electronic circuits. It is principally used as a voltage-controlled capacitor, and its diode capabilities are secondary. It is operated in reverse-biased so no current flows through it, but since the width of the depletion region varies with the applied bias voltage, the capacitance of the diode can vary.

Note that not all varactors are formed by diodes. In CMOS processes, varactors are formed by using the junctions of transistors to form a P-N junction device, thus, creating capacitance at these junctions. Varactors are commonly used in voltage-controlled oscillators as part of phase-locked loops and frequency synthesizers.

The varactor will be used as the variable capacitor for the MRI front-end system. Its purpose is to tune the microcoil at a resonant frequency of 200-MHz. The varactor designed is a CMOS transistor-based circuit, as shown in Figure 11. The varactor design in this thesis was done by Bo Shen, who is a Doctor of Philosophy candidate in the Electrical Engineering Department.
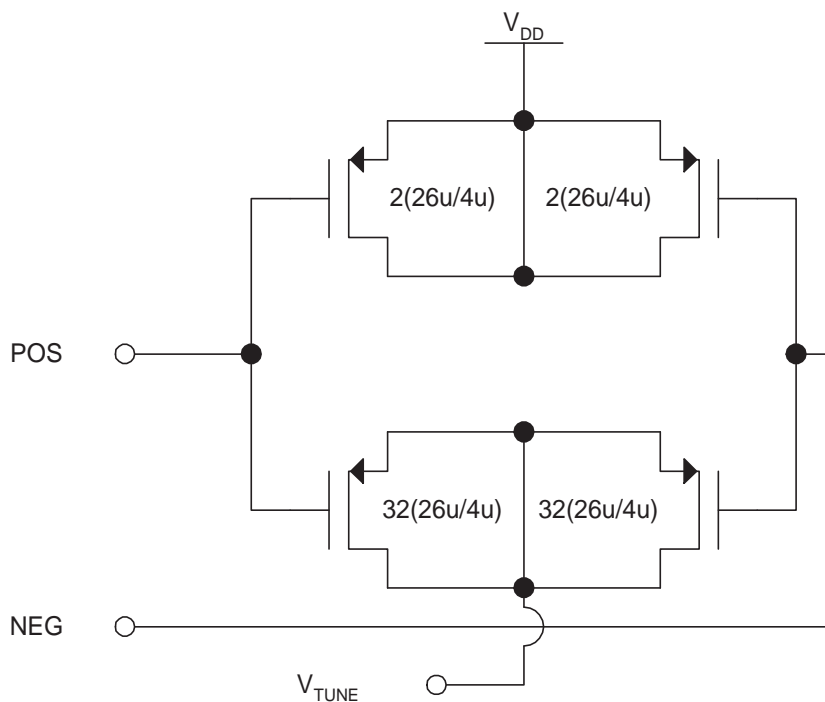
Fig. 11. Varactor Schematic (Courtesy of Bo Shen)

The tuning response of the varactor is shown in Figure 12. This figure shows the capacitance of the circuit as a function of the applied bias voltage. The varactor response shows a 250 mV tuning voltage range to get a 3.1 pF capacitance range.

Table IV shows the bias voltage and capacitance tuning ranges of the designed varactor.
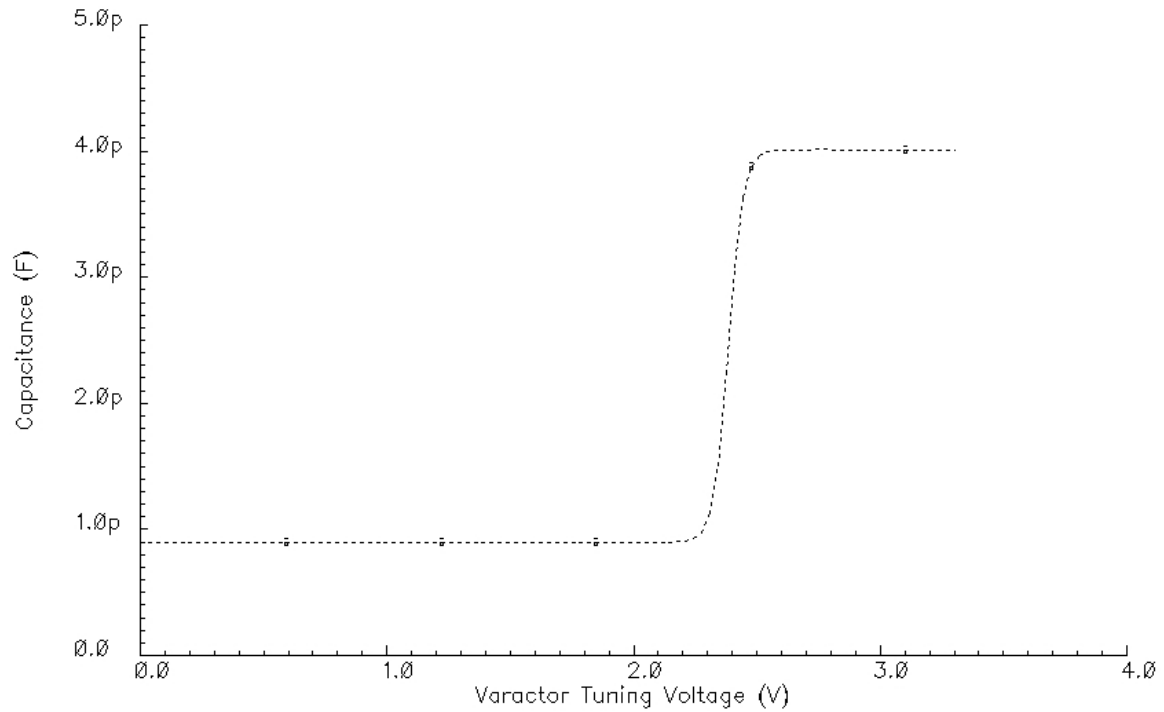
Fig. 12. Varactor Capacitance vs. Tuning Voltage Response

Table IV. Varactor Tuning Ranges

Tuning Range	Minimum	Maximum
Voltage (V)	2.20	2.55
Capacitance (pF)	0.90	4.00

CHAPTER III

PREAMPLIFIER

The preamplifier building block is designed to boost the signal strength while at the same time minimizing its own inherent noise into the MRI system. Since the incoming voltage seen across the microcoil circuit will be weak, the signal strength expected will be very low. In such a case, it is essential that the preamplifier provide a certain amount of gain while keeping the noise low.

A. Amplifier Architectures

The preamplifier required for the MRI system is designed to operate at much lower frequencies (200-MHz) than the conventional RF receiver which can range from 700-MHz to 3-GHz or possibly higher. In the design of low noise amplifiers, there are several common goals. These include minimizing the noise figure of the amplifier, providing gain with sufficient linearity, and providing a stable 50 Ω input impedance to terminate an unknown length of transmission line which delivers signal from the antenna to the amplifier. A good input match is more critical when a preselect filter precedes the LNA because such filters are often sensitive to the quality of their terminating impedances [12]. Table V shows three state-of-the-art LNA architectures that follow the common goals stated above and that provide some useful background to RF communications. Since the frequency requirements of the preamplifier for the MRI system are not as high as seen in Table V, a conventional RF communications approach may not be the best approach to take.

Table V. Summary of Recent LNA Results

Author [Ref.]	NF (dB)	Gain (dB)	f (GHz)	Technology
Karanicolas [13]	1.9	15.6	0.9	0.40-μm CMOS
Shaeffer & Lee [12]	3.5	22.0	1.5	0.60-μm CMOS
Nguyen & Lee [14]	1.7	18.9	5.2	0.18-μm CMOS

B.   Preamplifier Background and Specifications

A simple fully-differential amplifier with sufficient gain is the best option for the preamplifier block. Initially, the topology investigated for the preamplifier is a simple wideband amplifier, which is shown in Figure 13. Due to technology constraints, the maximum gain expected from this topology, or any other single-stage wideband amplifier, would not be greater than 20-dB. However, when the input signal is small, this gain may not be sufficient. Another issue with this type of topology is that there is a need to have a common-mode feedback system (CMFB) to adjust output DC levels. However, the CMFB system makes it difficult to achieve stability requirements of at least 45 degrees in phase margin.
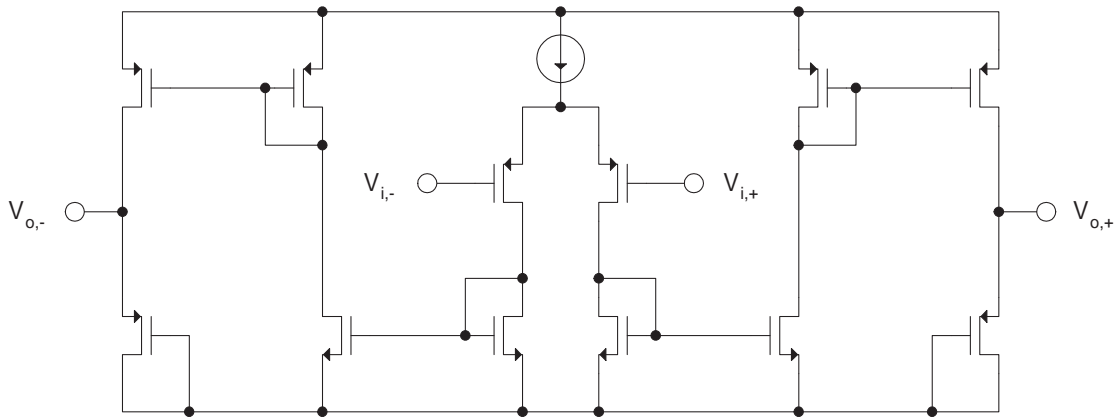
Fig. 13. Simple Wideband Amplifier Schematic

A common-mode feed-forward (CMFF) system is a popular option to combat the stability issues seen in a CMFB system. This complex topology will decrease the gain and increase active noise due to increase number of transistors. Also, the output voltage swing will be limited.

The preamplifier block will use a simple differential pair with resistive load that should give sufficient gain, if cascaded, with some low noise properties due to the small number of transistors and resistors. Although this architecture will not perform as well as an off-chip preamplifier seen on normal MRI systems, it will be sufficient for an initial prototype of the front-end system. A simple single-stage preamplifier with resistive load is shown in Figure 14. Since the DC level at the output is set by the resistors, a CMFB or CMFF system will not be required.
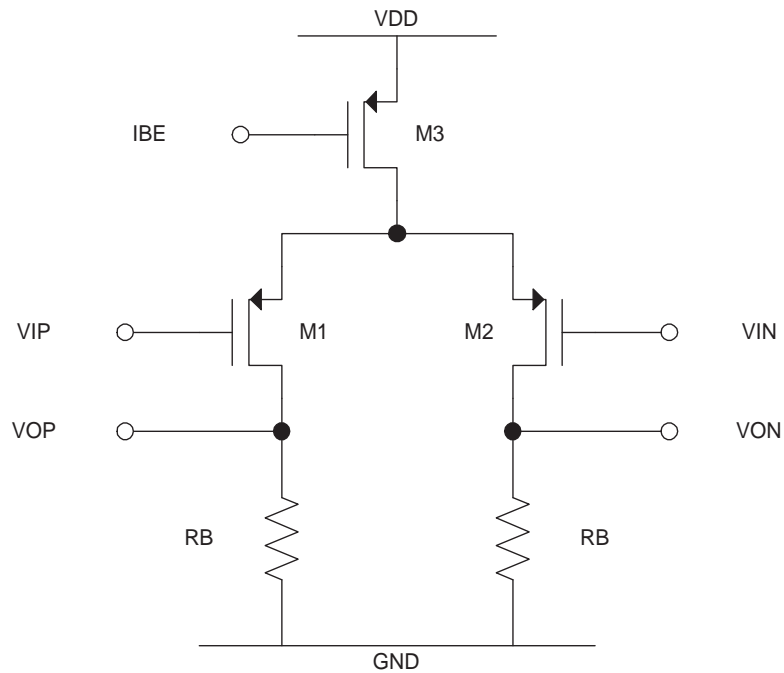
Fig. 14. Single-Stage Preamplifier Schematic

The gain of this topology is shown (3.1).

$$A_V = g_m \cdot R_B \tag{3.1}$$

The relation for g_m is shown in (3.2).

$$g_m = \sqrt{\mu_p \cdot C_{ox} \cdot \frac{W}{L} \cdot I_{RB}} \tag{3.2}$$

This indicates that for the PMOS input transistors, the current or the aspect ratio may be increased for a higher gain. However, increasing the ratio alone will not be a wise decision since parasitics associated with it may limit the bandwidth of the system. Power dissipation is not a stringent criterion; therefore, the system can withstand high currents for increased gain.

The specifications for the single-stage and three-stage preamplifier are shown in Table VI. The preamplifier will consist of three cascaded stages of equal value in gain.

Table VI. Preamplifier Specifications

Specifications	Single-Stage	Three-Stage
$\frac{1}{2} \cdot \mu_o \cdot C_{ox}$ (PMOS)	-32.7 $\frac{\mu A}{V}$	
V_t (PMOS)	-0.78 V	
A_V	15 dB	45 dB
3-dB Bandwidth	$\geq$ 200-MHz	$\geq$ 200-MHz
Noise	minimum	minimum
Output Voltage	1.65 V	1.65 V

C. Noise Analysis

In communication systems, it is known that the first block of a cascaded system, such as Figure 15, provides the maximum amount of noise overall. The overall system noise factor (F) for a cascaded system is given by (3.3) [7, 15].
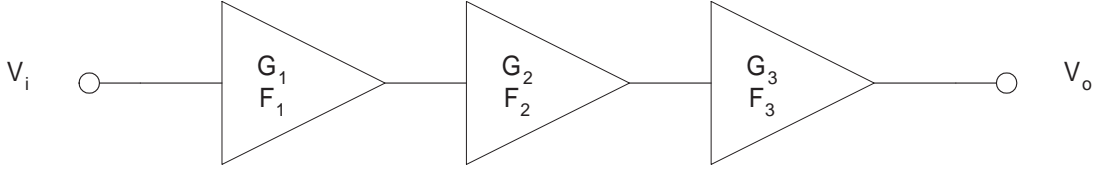
Fig. 15. Cascaded System Noise Analysis

$$F = F_1 + \frac{F_2 - 1}{G_1} + \frac{F_3 - 1}{G_1 \cdot G_2} \tag{3.3}$$

It is important to note that the gain of the first stage, although low, will produce low noise. The noise from the second stage is divided by the gain of the first stage and the noise of the third stage is divided by the gain product of the first and second stage. Although each stage of the preamplifier has approximately equal gain, the noise of the overall system will be approximately equal to the first stage.

It is critical to identify the noise sources to properly reduce the noise in the system. In this topology (Figure 14), the noise sources are the differential input pair and the resistors, while the current source seen in transistor M3 can be considered negligible [16]. For the input differential pair, the noise voltage is given by (3.5).

$$V_{n,out} = \frac{I_n}{2} \cdot R_B + \frac{I_n}{2} \cdot R_B = I_n \cdot R_B \tag{3.4}$$

$$V_{n,out}^2 = I_n^2 \cdot R_B^2 \tag{3.5}$$

The noise voltage for the resistor is seen in (3.6) and the noise current source is seen

in (3.7).

$$V_{n,RB}^2 \quad = \quad 4 \cdot k \cdot T \cdot R_B \tag{3.6}$$

$$I_n^2 \quad = \quad 4 \cdot k \cdot T \cdot \frac{2}{3} \cdot g_m \tag{3.7}$$

This gives the total output noise seen in (3.10).

$$V_{n,out}^2 \quad = \quad I_n^2 \cdot R_B^2 + V_{n,RB}^2 \tag{3.8}$$

$$= \quad 4 \cdot k \cdot T \cdot \frac{2}{3} \cdot g_m \cdot R_B^2 + 4 \cdot k \cdot T \cdot R_B \tag{3.9}$$

$$= \quad 4 \cdot k \cdot T \cdot \left(\frac{2}{3} \cdot g_m \cdot R_B^2 + R_B \right) \tag{3.10}$$

Dividing the result by the square of the differential gain, $g_m^2 \cdot R_B^2$, the input noise voltage can be calculated as seen in (3.11).

$$V_{n,in}^2 = 4 \cdot k \cdot T \cdot \left(\frac{2}{3 \cdot g_m} + \frac{1}{g_m^2 \cdot R_B} \right) \tag{3.11}$$

As seen in (3.10) and (3.11), increasing g_m will increase the output noise voltage and overall gain while reducing the input noise voltage. The noise factor of the system can be derived by the ratio of the input signal-to-noise ratio (SNR_{IN}) to the output signal-to-noise ratio (SNR_{OUT}) as shown in (3.12).

$$F = \frac{SNR_{IN}}{SNR_{OUT}} \tag{3.12}$$

SNR_{IN} is the mean square input signal voltage divided by the mean square input noise voltage from the microcoil.

$$SNR_{IN} = \frac{V_{IN}^2}{4 \cdot k \cdot T \cdot R_S} \tag{3.13}$$

$$R_S \Rightarrow \text{Input Resistance}$$

SNR_{OUT} is the mean square output signal voltage divided by the mean square output

noise voltage from the preamplifier.

$$SNR_{OUT} = \frac{A_V \cdot V_{IN}^2}{V_{n,out}^2} \tag{3.14}$$

$$= \frac{(g_m \cdot R_B \cdot V_{IN})^2}{4 \cdot k \cdot T \cdot \left(\frac{2}{3} \cdot g_m \cdot R_B^2 + R_B\right)} \tag{3.15}$$

$$= \frac{R_B \cdot (g_m \cdot V_{IN})^2}{4 \cdot k \cdot T \cdot \left(\frac{2}{3} \cdot g_m \cdot R_B + 1\right)} \tag{3.16}$$

Using (3.13) and (3.16), the noise factor simplifies into (3.17).

$$F = \frac{\frac{2}{3} \cdot g_m \cdot R_B + 1}{g_m^2 \cdot R_B \cdot R_S} \tag{3.17}$$

From (3.17), there will be a trade-off between the g_m in the preamplifier and the noise factor of the system since the resistances in the coil and preamplifier will be predetermined. The noise figure, the logarithmic version of noise factor, is shown in (3.18).

$$NF = 10 \cdot \log F \tag{3.18}$$

D. Amplifier Design

Using the specifications in Table VI and (3.2), the aspect ratio of the differential input pair can be derived as shown in (3.19).

$$\frac{W}{L} = \frac{g_m^2}{\mu_p \cdot C_{ox} \cdot I_{RB}} \tag{3.19}$$

Since each stage of the preamplifier is exactly the same, only a single-stage preamplifier will need to be design. The last two stages will be replicas in cascade. Table VII shows the calculated design values of a single-stage preamplifier.

Table VII. Single-Stage Preamplifier Design Values

Specification		Value	
$\mathbf{R}_S$		50-Ω	
$\mathbf{V}_{out}$		1.65-V	
$\mathbf{R}_B$		1-kΩ	
$\mathbf{I}_B$		1.65-mA	
$\mathbf{I}_{BE}$		3.30-mA	
$\mathbf{g}_m$		5.6-$\frac{mA}{V}$	
Transistor	W/L	L	W
Input Pair	400	0.4-μm	160-μm
Current	2500	0.4-μm	1000-μm

With the aid of (3.17) and Table VII, the noise factor and noise figure was calculated as shown in (3.20).

$$F = 3.02 \quad \Rightarrow \quad NF = 4.8 \quad \text{dB} \tag{3.20}$$

E.   Circuit Simulations

Figure 16 shows the frequency response of the single-stage preamplifier. The response shows a magnitude gain of 15.4 dB with a 3-dB bandwidth of 450-MHz. Table VIII shows the noise summary of a single-stage preamplifier. As expected, the differential input pair carries the majority of the noise contribution. A 100-μV, 200-MHz sinusoidal signal was applied to the system. Figure 17 shows the response from this input signal as approximately a 0.55-mV, 200-MHz signal.
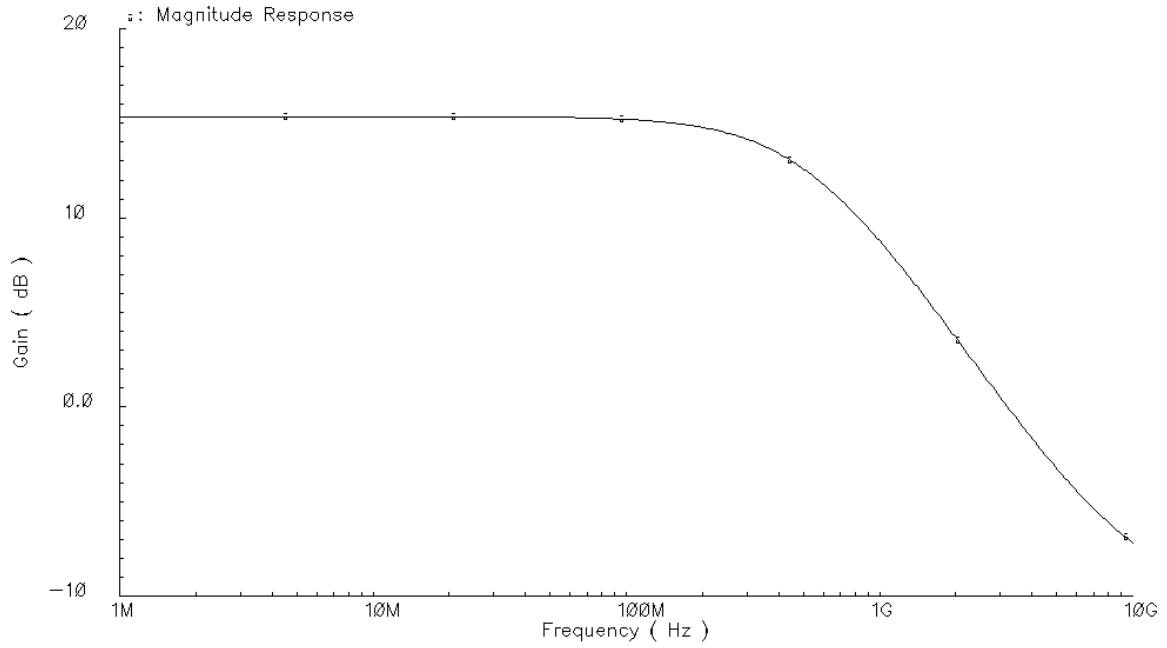
Fig. 16. Single-Stage Preamplifier Magnitude Response

Table VIII. Single-Stage Preamplifier Noise Summary

Device	Contribution (pV)	Percentage (%)
M1	264.038	43.07
M2	264.038	43.07
RB1	42.479	6.93
RB2	42.479	6.93
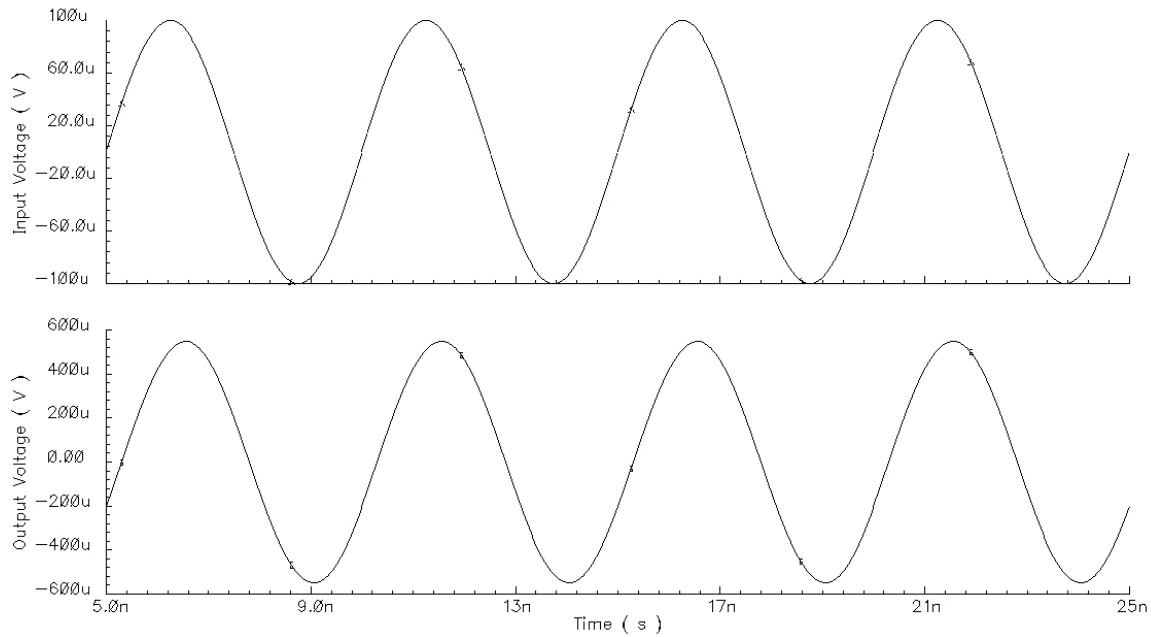
Fig. 17. Single-Stage Preamplifier Transient Response at 200-MHz

Figure 18 shows the frequency response of the three-stage preamplifier. The response shows a magnitude gain of 46.1 dB with a 3-dB bandwidth of 241-MHz. Table IX shows the noise summary of the three-stage preamplifier. The noise summary follows (3.3) by indicating that the differential input pair of Stage 1 carries the majority of the noise contribution. A 100-μV, 200-MHz sinusoidal signal was applied to the system. Figure 19 shows the response from this input signal as approximately an 11.41-mV, 200-MHz signal.

F.   Layout Considerations

The floorplan of the preamplifier has three major blocks, which use proper layout techniques for transistors and resistors. The current mirrors of the block were of the same width with a factor of 4 multipliers. This allowed for the current mirror block to be drawn common-centroid to reduce cross-chip temperature gradients and provide
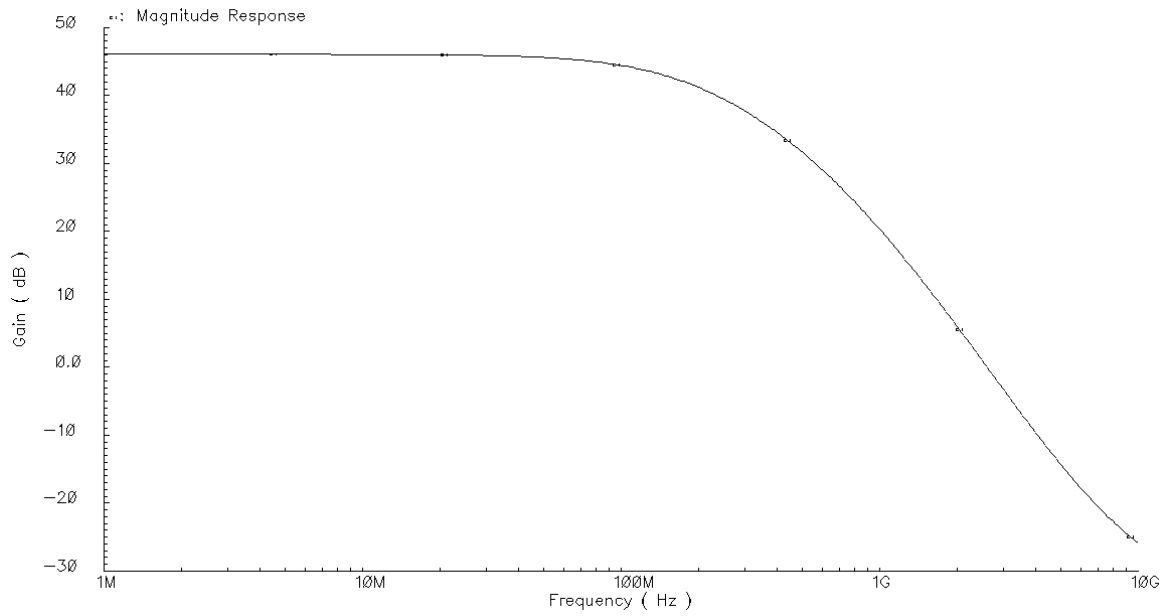
Fig. 18. Three-Stage Preamplifier Magnitude Response

Table IX. Three-Stage Preamplifier Noise Summary

Stage	Device	Contribution (nV)	Percentage (%)
1	M1	114.427	41.41
1	M2	114.427	41.41
1	RB1	18.397	6.66
1	RB2	18.397	6.66
2	M1	4.386	1.59
2	M2	4.386	1.59
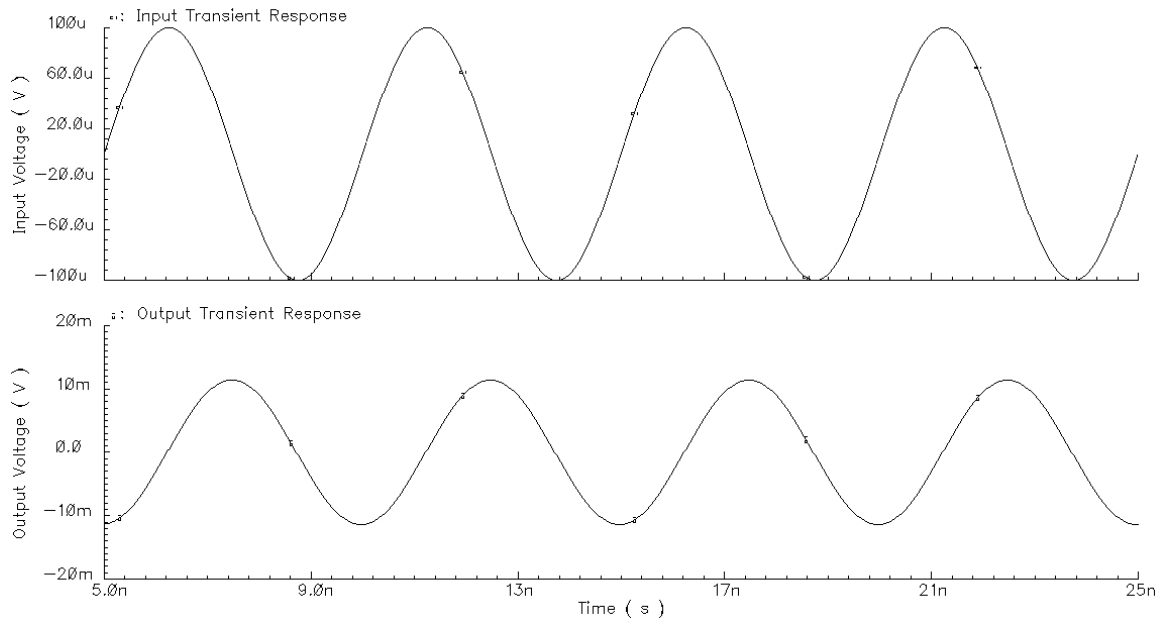
Fig. 19. Three-Stage Preamplifier Transient Response at 200-MHz

good matching. Each differential input stage was of the same width with a factor of 20 multiplier. Each stage was drawn in its own mini-block and drawn common-centroid. Dummy transistors were placed on the outside of each block to reduce mismatch. The resistors were laid out in POLY2 in units of 250-Ω to reduce mismatching. This created 8 units of POLY2 blocks for each stage's two 1-kΩ resistors. The resistors were drawn in common-centroid with dummy resistors. All horizontal interconnecting was done using metal 1 and all vertical interconnecting was done using metal 2. Ground connections filled in empty areas to help create a good-looking rectangular block for top-level layout. Figure 20 shows the layout of the preamplifier block.
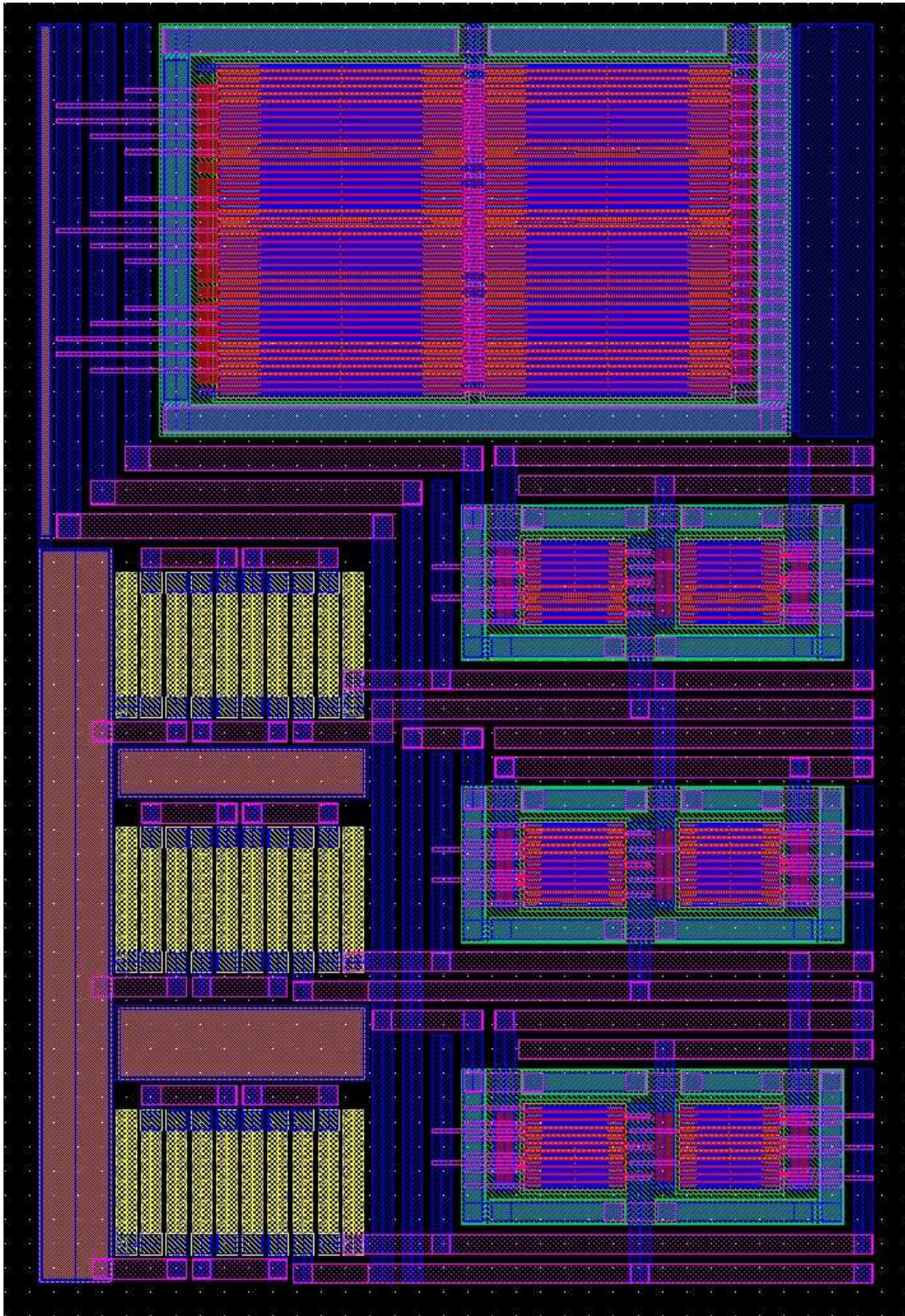
Fig. 20. Three-Stage Preamplifier Layout

CHAPTER IV

BANDPASS FILTER

Filters are essential components in many electrical systems. In state-of-the-art RF receivers, high performance filters are required to remove undesired signals at different stages of the receiving process, such as noise from incoming signals the antenna receives, undesired signals at the image frequency, and harmonics after the mixing operation.

For this research, the MRI front-end system will need a bandpass filter to reject the undesired signals at the image frequency. Since the RF signal generated by the MRI system is clean, the need for other filter blocks seen in general RF receivers will not be required.

A.   Filter Background and Specifications

An electrical filter is a two-port device that modifies the magnitude and phase of the input signal to produce a desired output signal. In this case, a signal can be considered as a collection of signals at various frequencies. There are two types of frequency bands that are strictly defined over the frequency of interest. An ideal filter will transmit or amplify signals in the passband, while it will attenuate or reject the signals in the stopband. Depending on the allocation of the pass and stop frequency bands, filters can be classified as lowpass, highpass, bandpass, or bandstop [17].

A bandpass filter is desired for the front-end system because all signals outside the 200-MHz time-varying signal produced by the MRI system need to be rejected. Bandpass filters passes frequencies in a desired range and attenuates frequencies below and above this range. All bandpass filter functions are at least second-order systems, as seen in Figure 21.
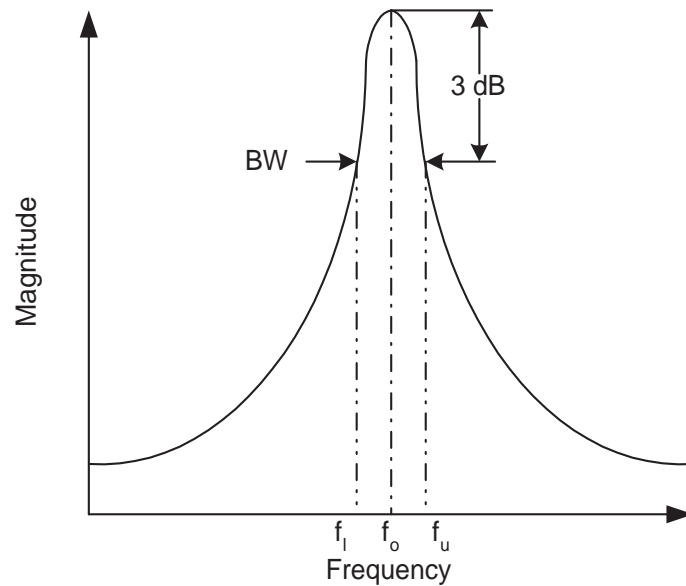
Fig. 21. Second-Order Bandpass Filter Response

A second-order bandpass filter can be characterized by its center frequency and its 3-dB bandwidth. The center frequency, ω_o, is the frequency at which the peak gain occurs.

$$\omega_o = 2 \cdot \pi \cdot f_o \tag{4.1}$$

The 3-dB frequencies, f_l and f_u, are defined as the frequencies where the peak gain drops by 3 dB. The 3-dB bandwidth, BW, is determined by the difference of the 3-dB frequencies.

$$BW = f_u - f_l \tag{4.2}$$

The quality factor is defined as the ratio of the center frequency to the bandwidth.

$$Q = \frac{\omega_o}{2 \cdot \pi \cdot BW} = \frac{f_o}{f_u - f_l} \tag{4.3}$$

The parameters of peak gain (H), center frequency (ω_o), and quality factor (Q) forms

a general second-order system bandpass transfer function seen in (4.4).

$$\frac{V_B}{V_I} = H \cdot \frac{\frac{\omega_o}{Q} \cdot s}{s^2 + \frac{\omega_o}{Q} \cdot s + {\omega_o}^2} \tag{4.4}$$

In a second-order filter case, more attenuation in the stopband cannot be achieved for a given bandwidth and center frequency, which means as Q is increased for more attenuation, the bandwidth of the filter will decrease. A high-order filter can achieve this increase in attenuation for a fixed bandwidth. Figure 22 shows the filter response of a high-order bandpass system.
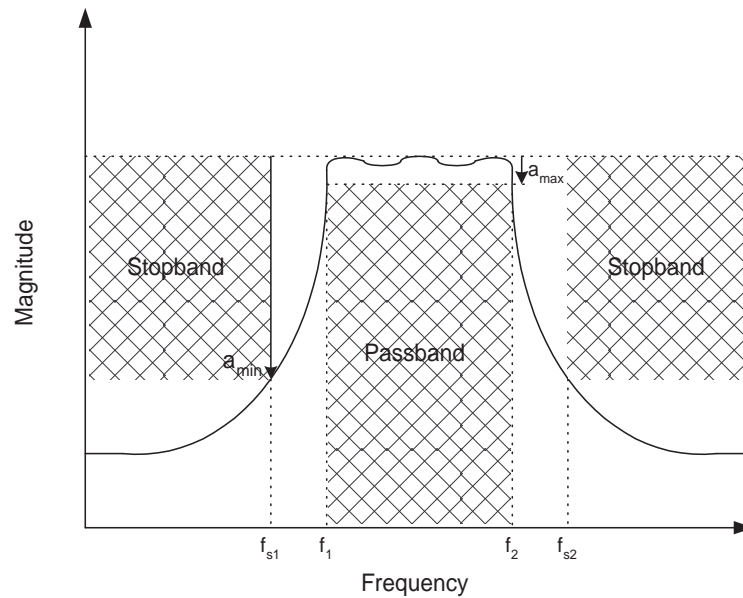
Fig. 22. High-Order Bandpass Filter Response

For a high-order system, attenuation in the pass and stop frequency bands have to satisfy the requirements seen in (4.5) and (4.6).

$$a_{max} \geq a(f) \qquad \text{for} f_1 \leq f \leq f_2 \tag{4.5}$$

$$a_{min} \leq a(f) \qquad \text{for} f \leq f_{s1}, f \geq f_{s2} \tag{4.6}$$

The attenuation with respect to maximum gain in the passband is defined by $a(f)$, in dB units. The passband frequencies are defined by f_1 and f_2 while the stopband frequencies are defined by f_{s1} and f_{s2}. The passband ripple, a_{max}, and the stopband attenuation, a_{min}, are defined as the maximum allowed attenuation in the passband and the minimum required attenuation in the stopband, respectively [18].

The high-order bandpass filter is a response that meets the needs of the filter required for the MRI front-end system. For the system, there are strict requirements in pass frequency bandwidth and the maximum attenuation allowed in the passband. Table X illustrates the specifications for the bandpass filter.

Table X. Bandpass Filter Specifications

Center Frequency	200-MHz	
Passband Frequencies	197.5-MHz	202.5-MHz
Stopband Frequencies	170.0-MHz	230.0-MHz
Passband Ripple	0.1 dB	
Stopband Attenuation	30 dB	

The specifications seen in Table X will factor into the decision of the type of implementation used to design this filter. Different circuit architectures will be discussed and a magnitude approximation technique will be used to determine coefficient values for a specific architecture.

B. Filter Architectures

It should be noted that a high-order filter response is a system of cascading second-order filter blocks. For this reason, it necessary to become familiar with some basic second-order filter architectures. A system diagram is a useful tool to help generate

a circuit implementation of any circuit block. Therefore, a system level analysis will be performed for a general second-order filter. From this system analysis, circuit implementations like active-RC, transconductance-C, and others can be derived.

1. System Level Analysis

Every filter architecture discussed in this chapter originates from a simple system diagram based on a two-integrator loop, which ensures system stability. This type of structure is called a Tow-Thomas Biquad. Figure 23 shows this general second-order filter system based on the two-integrator loop biquad structure [17].
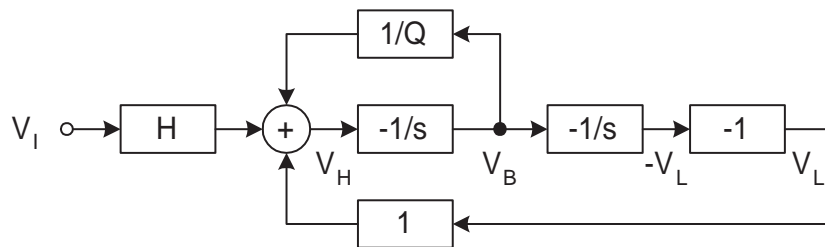
Fig. 23. General Second-Order Filter System Diagram

Variables V_I, V_H, V_B, and V_L represent the input signal, the highpass output, the bandpass output, and the lowpass output, respectively. From the system diagram, the following four basic equations can be formed that will help derive the filter functions:

$$V_H = H \cdot V_I + V_L + \frac{1}{Q} \cdot V_B \tag{4.7}$$

$$V_B = -\frac{1}{s} \cdot V_H \tag{4.8}$$

$$-V_L = -\frac{1}{s} \cdot V_B \tag{4.9}$$

$$V_L = -1 \cdot -V_L \tag{4.10}$$

Manipulating (4.8) into (4.7) will give a detailed bandpass output, seen in (4.11),

that will be used in the Active-RC circuit implementation.

$$V_B = -\frac{Q}{1 + s \cdot Q} \cdot (V_L + H \cdot V_I) \tag{4.11}$$

Manipulating (4.9) into (4.11) gives the general normalized voltage function of a bandpass filter, seen in (4.12).

$$V_B = -H \cdot Q \cdot \frac{\frac{1}{Q} \cdot s}{s^2 + \frac{1}{Q} \cdot s + 1} \cdot V_I \tag{4.12}$$

Manipulating (4.12) into (4.9) gives the general normalized voltage function of a lowpass filter, seen in (4.13).

$$V_L = -H \cdot \frac{1}{s^2 + \frac{1}{Q} \cdot s + 1} \cdot V_I \tag{4.13}$$

Using a few of these equations, circuit implementations can be derived from this system level analysis.

2.   Active-RC Implementation

An active-RC implementation of a second-order system response can be done using a few equations from the previous section. These equations have functions of simple circuit structures that can be implemented using operational amplifiers, resistors, and capacitors. Figure 23 can be realized using the active-RC implementation with (4.9), (4.10), and (4.11) [19].

- (4.11) is an inverting lossy integrator.

- (4.9) is an inverting integrator.

- (4.10) is an inverter.

   Combining these equations and making connections suggested by the input-output labels of the equations of the three blocks results in the full circuit seen

in Figure 24. The circuit cannot realize the highpass output because the summing block has been merged with the first integrator.
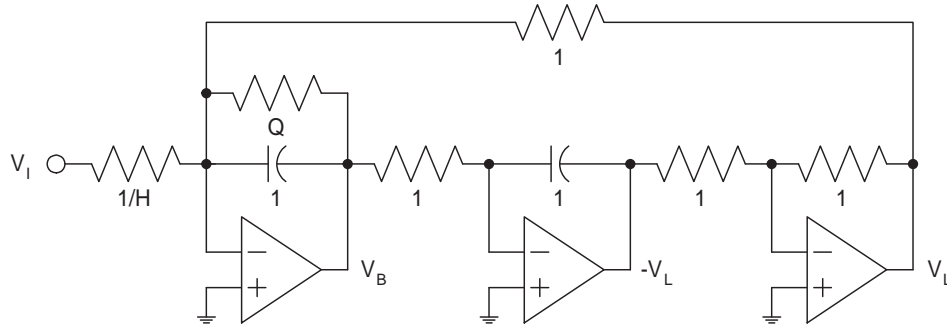
Fig. 24. Normalized Single-Ended Second-Order Active-RC Filter

Replacing the normalized values of the passive elements in Figure 24 with variables, a routine analysis can be done to find the transfer functions for each response.

Fig. 25. General Single-Ended Second-Order Active-RC Filter

There are two design equations that are derived from Figure 25 that will determine all transfer functions. The first equation is based on Kirchoff's Current Law at the negative node of the first operational amplifier and the second equation is an inverting transfer function of the second operational amplifier. The third operational

amplifier is simply an inverting amplifier for the lowpass output. The two design equations are:

$$\frac{V_I}{R_1} = \frac{-V_L}{R_5} + \frac{-V_B}{R_2} + \frac{-V_B}{\frac{1}{s \cdot C_1}} \tag{4.14}$$

$$V_L = \frac{1}{s \cdot R_4 \cdot C_2} \cdot V_B \tag{4.15}$$

Solving for V_B from (4.15) and manipulating into (4.14) gives the lowpass transfer function, seen in (4.16).

$$\frac{V_L}{V_I} = -\frac{R_5}{R_1} \cdot \frac{\frac{1}{R_4 \cdot R_5 \cdot C_1 \cdot C_2}}{s^2 + \frac{1}{R_2 \cdot C_1} \cdot s + \frac{1}{R_4 \cdot R_5 \cdot C_1 \cdot C_2}} \tag{4.16}$$

Manipulating (4.15) into (4.14) gives the bandpass transfer function, seen in (4.17).

$$\frac{V_B}{V_I} = -\frac{R_2}{R_1} \cdot \frac{\frac{1}{R_2 \cdot C_1} \cdot s}{s^2 + \frac{1}{R_2 \cdot C_1} \cdot s + \frac{1}{R_4 \cdot R_5 \cdot C_1 \cdot C_2}} \tag{4.17}$$

From (4.17), the important parameters of a bandpass filter can be derived using (4.4). These parameters are shown in (4.18), (4.19), and (4.20).

$$H = -\frac{R_2}{R_1} \tag{4.18}$$

$$\omega_o = \sqrt{\frac{1}{R_4 \cdot R_5 \cdot C_1 \cdot C_2}} \tag{4.19}$$

$$Q = \sqrt{\frac{R_2^2 \cdot C_1}{R_4 \cdot R_5 \cdot C_2}} \tag{4.20}$$

Since operational amplifiers are limited due to their internal bandwidth, it is not ideal for filters at moderately high frequencies. The frequency needed for the filter block of the MRI system is a few hundred megahertz, whereas, operational amplifiers' bandwidth is in the range of a few megahertz. Also, passive capacitors tend to be large in size for active-RC filters that are not ideal in integrated circuit fabrication. Last, passive resistors have a large mismatch due to process variations. Therefore,

another circuit implementation is required for the operation of this filter.

3. Transconductance-C Implementation

Transconductance-C, also called G_m-C, filters uses the same methods that are used in the active-RC filters. These types of filters are normally designed for operation at much higher frequencies than circuits built with operational amplifiers with some slight differences. There are no passive resistors used for this implementation and capacitors are much smaller, in the order of a few picofarads or less.

The transconductance-C filter uses the same system level diagram excluding the final inverting block. Therefore, only an integrator cascaded with a lossy integrator feeding back into the first integrator. Figure 26 shows a single-ended G_m-C filter circuit [20].
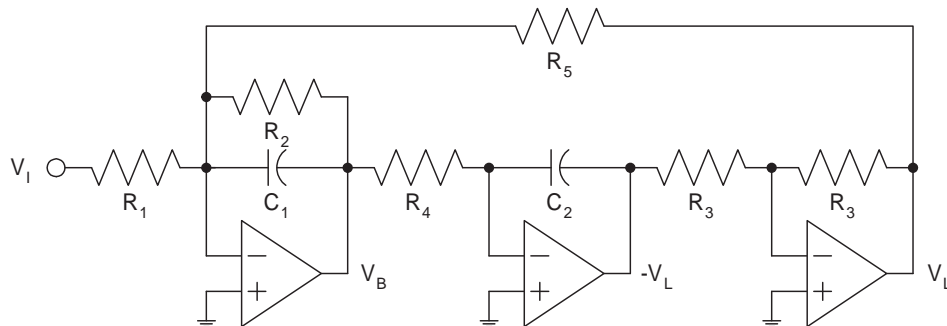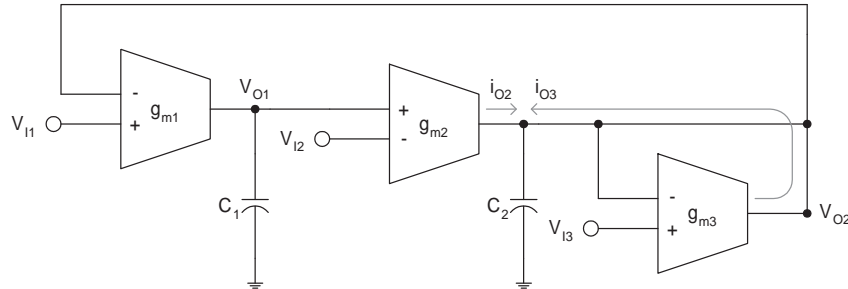

Fig. 26. General Single-Ended Second-Order G_m-C Filter

There are four design equations that are derived from Figure 26 that will determine the transfer functions. These equations are shown in (4.21), (4.22), (4.23), and

(4.24).

$$V_{O1} = g_{m1} \cdot (V_{I1} - V_{O2}) \cdot \frac{1}{s \cdot C_1} \tag{4.21}$$

$$V_{O2} = \frac{1}{s \cdot C_2} \cdot (i_{O2} + i_{O3}) \tag{4.22}$$

$$i_{O2} = g_{m2} \cdot (V_{O1} - V_{I2}) \tag{4.23}$$

$$i_{O3} = g_{m3} \cdot (V_{I3} - V_{O2}) \tag{4.24}$$

Manipulating (4.22), (4.23), and (4.24) into (4.21), V_{O1} is derived in (4.25).

$$V_{O1} = \frac{\left(\frac{g_{m1}}{C_1} \cdot s + \frac{g_{m1} \cdot g_{m3}}{C_1 \cdot C_2}\right) \cdot V_{I1} + \frac{g_{m1} \cdot g_{m2}}{C_1 \cdot C_2} \cdot V_{I2} - \frac{g_{m1} \cdot g_{m3}}{C_1 \cdot C_2} \cdot V_{I3}}{s^2 + \frac{g_{m3}}{C_2} \cdot s + \frac{g_{m1} \cdot g_{m2}}{C_1 \cdot C_2}} \tag{4.25}$$

Manipulating (4.21), (4.23), and (4.24) into (4.22), V_{O2} is derived in (4.26).

$$V_{O2} = \frac{\frac{g_{m1} \cdot g_{m2}}{C_1 \cdot C_2} \cdot V_{I1} - \frac{g_{m2}}{C_2} \cdot s \cdot V_{I2} + \frac{g_{m3}}{C_2} \cdot s \cdot V_{I3}}{s^2 + \frac{g_{m3}}{C_2} \cdot s + \frac{g_{m1} \cdot g_{m2}}{C_1 \cdot C_2}} \tag{4.26}$$

(4.25) and (4.26) provide a few different types of lowpass and bandpass filter functions with a common center frequency and quality function. Based on these two equations, the center frequency and quality factor functions are:

$$\omega_o = \sqrt{\frac{g_{m1} \cdot g_{m2}}{C_1 \cdot C_2}} \tag{4.27}$$

$$\frac{\omega_o}{Q} = \frac{g_{m3}}{C_2} \tag{4.28}$$

$$Q = \sqrt{\frac{g_{m1} \cdot g_{m2}}{g_{m3}^2} \cdot \frac{C_2}{C_1}} \tag{4.29}$$

(4.26) provides two bandpass filter functions that meet the needs of the filter block for this system.

1. With V_{I1} and V_{I3} grounded, (4.26) becomes a bandpass filter function with gain.

$$H = -\frac{g_{m2}}{g_{m3}} \tag{4.30}$$

2. With V_{I1} and V_{I2} grounded, (4.26) becomes a bandpass filter function with unity gain.

$$H = 1. \tag{4.31}$$

The best circuit implementation is Figure 26 with V_{I1} and V_{I3} grounded to have the ability to provide gain to the bandpass filter. Since the MRI front-end system is designed to be fully-differential, Figure 26 needs to be transformed into a fully-differential circuit. The fully-differential transformation of the single-ended second-order G_m-C filter can be seen in Figure 27.

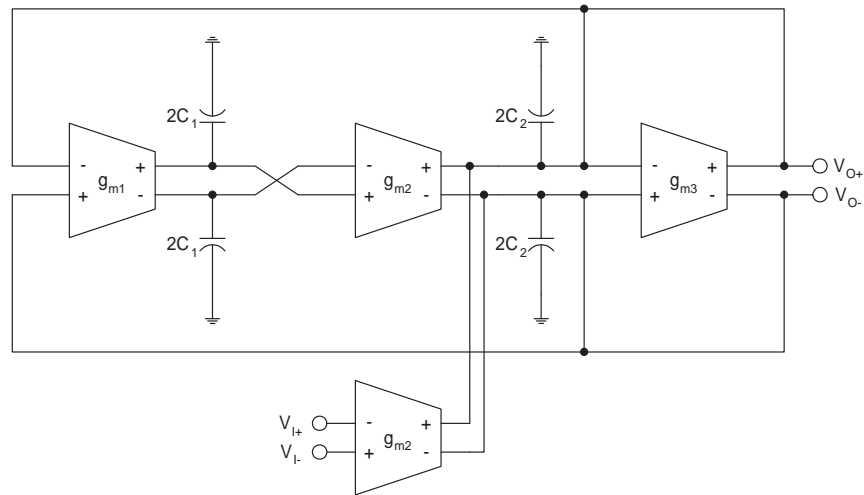Fig. 27. Fully-Differential Second-Order G_m-C Filter

C. Filter Design

A high-order bandpass filter can be designed using different magnitude approximation techniques, such as Butterworth or Chebyshev based on the allocation of poles. These approximations are not types of filters but rather types of filter responses. There are many software tools available to synthesize a filter with these different approximation

methods.

The Butterworth approximation is a filter response with no signal ripple in the passband but usually sacrifices some steepness in attenuation in the stopband. The Chebyshev approximation is a filter response that allows some signal ripple, usually between 0.1-dB and 3-dB, in the passband but allows an attenuation slope that is steeper than a Butterworth approximation.

Since the specifications are strict in terms of the passband ripple and the stopband attenuation, the Chebyshev approximation will be the best method to use in the designing the bandpass filter. The filter design method follows a procedure taught in an operational amplifier/filter graduate course. The passband and stopband frequency specifications (converted from MHz to rad/s) for the bandpass filter are shown below.

$$\omega_{p1} = 2 \cdot \pi \cdot f_{p1} = 2 \cdot \pi \cdot 197.5 \cdot 10^6 = 395 \cdot 10^6 \cdot \pi \tag{4.32}$$

$$\omega_{p2} = 2 \cdot \pi \cdot f_{p2} = 2 \cdot \pi \cdot 202.5 \cdot 10^6 = 405 \cdot 10^6 \cdot \pi \tag{4.33}$$

$$\omega_{s1} = 2 \cdot \pi \cdot f_{s1} = 2 \cdot \pi \cdot 170.0 \cdot 10^6 = 340 \cdot 10^6 \cdot \pi \tag{4.34}$$

$$\omega_{s2} = 2 \cdot \pi \cdot f_{s2} = 2 \cdot \pi \cdot 230.0 \cdot 10^6 = 460 \cdot 10^6 \cdot \pi \tag{4.35}$$

The resonant frequency and quality factor of the filter are shown in (4.36) and (4.37).

$$f_o = \sqrt{f_{p1} \cdot f_{p2}} \Rightarrow \omega_o = 2 \cdot \pi \cdot f_o = 400 \cdot 10^6 \cdot \pi \tag{4.36}$$

$$Q = \frac{\omega_o}{\omega_{p2} - \omega_{p1}} = 40 \tag{4.37}$$

The stopband frequencies are normalized to the resonant frequency.

$$\omega'_{s1} = \frac{\omega_{s1}}{\omega_o} = 0.8501 \tag{4.38}$$

$$\omega'_{s2} = \frac{\omega_{s2}}{\omega_o} = 1.1501 \tag{4.39}$$

New prototype stopband frequencies will be derived from the normalized stopband frequencies.

$$\Omega_{s1} = Q \cdot \left| \frac{\omega_{s1}'^2 - 1}{\omega_{s1}'} \right| = 13.0515 \tag{4.40}$$

$$\Omega_{s2} = Q \cdot \left| \frac{\omega_{s2}'^2 - 1}{\omega_{s2}'} \right| = 11.2228 \tag{4.41}$$

Using the maximum passband ripple (α_{max}), the minimum stopband attenuation (α_{min}), a prototype passband frequency of 1 ($\Omega_p = 1$), and one of the new prototype stopband frequencies (Ω_s), a lowpass prototype filter can be derived. The higher filter order, n, will be required from either of the prototype stopband frequencies.

$$n = \frac{cosh^{-1} \sqrt{\frac{10^{0.1 \cdot \alpha_{min}} - 1}{10^{0.1 \cdot \alpha_{max}} - 1}}}{cosh^{-1} \left(\frac{\Omega_{s1}}{\Omega_p} \right)} = 1.8482 \tag{4.42}$$

$$n = \frac{cosh^{-1} \sqrt{\frac{10^{0.1 \cdot \alpha_{min}} - 1}{10^{0.1 \cdot \alpha_{max}} - 1}}}{cosh^{-1} \left(\frac{\Omega_{s2}}{\Omega_p} \right)} = 1.9383 \tag{4.43}$$

In either prototype stopband frequency case, the lowpass prototype filter order will be: $n = 2$. The constants required for the filter approximations are shown in (4.44) and (4.45).

$$\epsilon = \sqrt{10^{0.1 \cdot \alpha_{min}} - 1} = 0.1526 \tag{4.44}$$

$$a = \frac{1}{n} \cdot sinh^{-1} \frac{1}{\epsilon} = 1.2894 \tag{4.45}$$

The poles of the lowpass prototype filter system, for $k = 1 \ldots \frac{n}{2}$, are shown in (4.48).

$$\psi_k = \frac{\pi}{n} \cdot k - \frac{\pi}{2 \cdot n} = \frac{\pi}{4} \tag{4.46}$$

$$s = -(sinh \quad a \cdot cos \quad \psi_k) \pm j \cdot (cosh \quad a \cdot sin \quad \psi_k) \tag{4.47}$$

$$s = -1.1862 \pm j \cdot 1.3810 \tag{4.48}$$

The resonant frequency and quality factor of the lowpass prototype filter are shown in (4.49) and (4.50).

$$\omega_o' = |s| = 1.8205 \tag{4.49}$$

$$Q' = \frac{\omega_o'}{2 \cdot (sinh \quad a \cdot cos \quad \psi_k)} = 0.7674 \tag{4.50}$$

The lowpass prototype transfer function is shown in (4.51).

$$H_{LP}(s) = \frac{\omega_o'^2}{s^2 + \frac{\omega_o'}{Q'} \cdot s + \omega_o'^2} = \frac{3.3142}{s^2 + 2.3723 \cdot s + 3.3142} \tag{4.51}$$

Substituting (4.52) into the lowpass prototype transfer function (4.51) will transform and denormalize into the bandpass transfer function.

$$s \rightarrow Q \frac{(s/\omega_o)^2 + 1}{s/\omega_o} = 31.8310 \cdot 10^{-9} \cdot s + \frac{50.2576 \cdot 10^9}{s} \tag{4.52}$$

After the bandpass transformation and denormalization of the lowpass prototype, (4.53) shows the final bandpass filter transfer function.

$$H_{BP}(s) =$$

$$\underbrace{1.5350 \frac{37.9073 \cdot 10^6 \cdot s}{s^2 + 37.9073 \cdot 10^6 \cdot s + 1.6343 \cdot 10^{18}}}_{\text{Stage 1}} \cdot \underbrace{1.5350 \frac{36.6206 \cdot 10^6 \cdot s}{s^2 + 36.6206 \cdot 10^6 \cdot s + 1.5252 \cdot 10^{18}}}_{\text{Stage 2}}$$

$$\tag{4.53}$$

$$\text{Stage 1: } H_1 = 1.535, \quad f_{o1} = 203.467 \quad \text{MHz}, \quad Q_1 = 33.725$$

$$\text{Stage 2: } H_1 = 1.535, \quad f_{o2} = 196.561 \quad \text{MHz}, \quad Q_2 = 33.725$$

Figure 28 verifies the bandpass filter transfer function using MATLAB with all the requirements within the design specifications.

After MATLAB verification, a macromodel verification is needed to prove that the $G_m - C$ filter architecture (Figure 27) will follow the bandpass transfer function de-
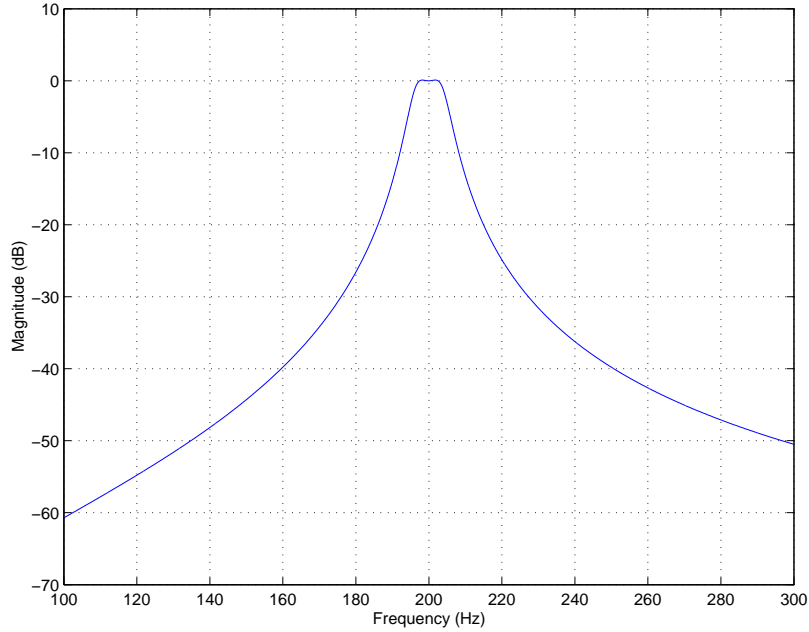
Fig. 28. MATLAB Filter Frequency Response

signed by the Chebyshev approximation. For macromodel simulations, the transconductors in the architecture are replaced with voltage-controlled current sources with the transconductance values calculated from (4.27), (4.28), and (4.30) and $C = C_1 = C_2 = 1$-pF. The calculated transconductance values for each stage of the $G_m - C$ Filter is shown in Table XI. The macromodel simulation of the bandpass filter is shown in Figure 29, which shows the design is within design specifications.

Table XI. G_m-C Filter Transconductances

Transconductor	Equation	Stage 1	Stage 2
g_{m3}	$\frac{\omega_o}{Q} \cdot C$	37.91 $\frac{\mu A}{V}$	36.62 $\frac{\mu A}{V}$
g_{m2}	$H \cdot g_{m3}$	58.19 $\frac{\mu A}{V}$	56.21 $\frac{\mu A}{V}$
g_{m1}	$\frac{C^2}{g_{m2}} \cdot \omega_o^2$	28.09 $\frac{mA}{V}$	27.13 $\frac{mA}{V}$

Figure 29 illustrates a good preliminary design of the $G_m - C$ bandpass filter that will meet the needs of the MRI system. With transconductances of each operational transconductance amplifier (OTA) calculated, the next step is to design the OTA according to those values. Unfortunately, due to high noise properties of active devices and time constraints, the bandpass filter block of the MRI system had to be eliminated.
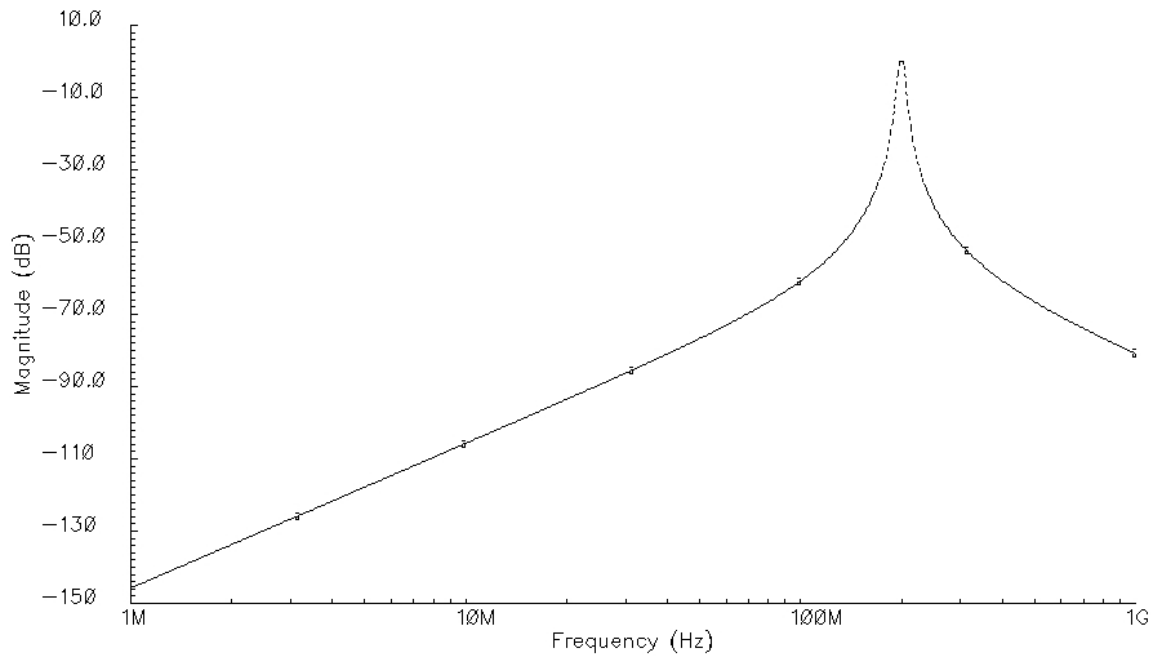
Fig. 29. Macromodel Frequency Response

CHAPTER V

MRI SYSTEM ANALYSIS

After each block has been individually discussed and designed, the blocks were put together and analyzed as a system through simulations and experimental tests. First, the MRI system was simulated to meet the specifications similar to that of the microcoil and preamplifier blocks. Then, the system was carefully laid out using the standard TSMC 0.35-μm CMOS Technology. Lastly, experimental measurements were conducted to verify the functionality of the system after integrated circuit fabrication.

A. System Level Analysis

Figure 5 is the basis for the single-channel MRI system. Using the designs for the microcoil, varactor, and preamplifier together, a system simulation was performed to meet the required specifications.

1. System Level Simulations

First, a frequency response simulation was performed on the single-channel MRI system. It is expected to see a similar a frequency response seen from the parallel-tuned microcoil (Figure 9) with a 40-dB gain from the preamplifier. Figure 30 shows the MRI system frequency response and Table XII shows that the system meets the expected specifications.
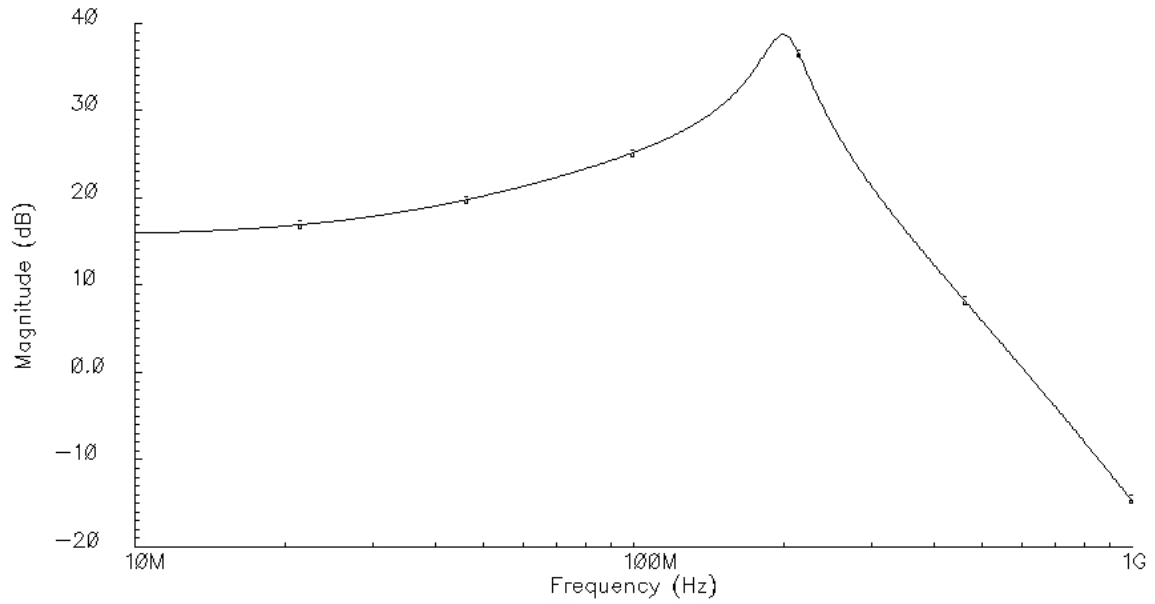
Fig. 30. MRI System Frequency Response

Table XII. MRI System Simulation Results

Resonant Gain	39.5 dB
Resonant Frequency	199.5-MHz
Lower 3-dB Frequency	182.2-MHz
Upper 3-dB Frequency	217.5-MHz
Quality Factor	5.6516

Since the system is designed to operate at 200-MHz, a transient response simulation was performed to verify functionality in the time domain. A 100-μV, 200-MHz sinusoidal signal was applied to the system. Figure 31 shows the response from this input signal as approximately a 9.5-mV, 200-MHz signal.
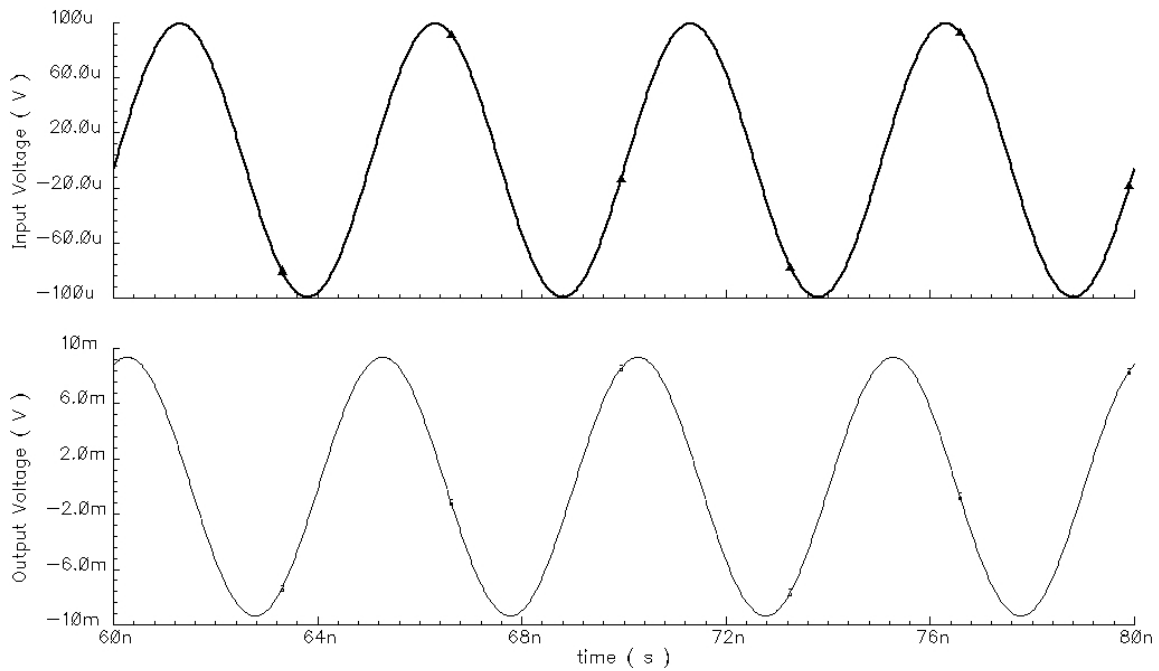
Fig. 31. MRI System Transient Response at 200-MHz

2. System Layout Considerations

Before considering the layout of the entire integrated circuit, it is necessary to discuss the single-channel system layout. The single-channel system layout consists of the layouts of the microcoil, varactor, and preamplifier. The varactor and preamplifier are placed adjacent to each other and underneath the microcoil. All horizontal interconnecting was done using metal 1 and all vertical interconnecting was done using

metal 2. In order to provide some isolation from the other channel of the MRI system, three guard rings are put around each channel. Each guard ring is 20-μm wide with 20-μm separation from one another. The inner most ring is a p+ ring tied to the analog ground of the IC. The middle ring is an n-well ring tied to the power supply of the IC. Last, the outer most ring is a p+ ring tied to the analog ground of the channel. All unused area was filled in using polysilicon and metals 1 & 2. The entire channel with the exception of the microcoil was covered in metals 3 & 4. Figure 32 shows the layout of a single-channel for the MRI system.
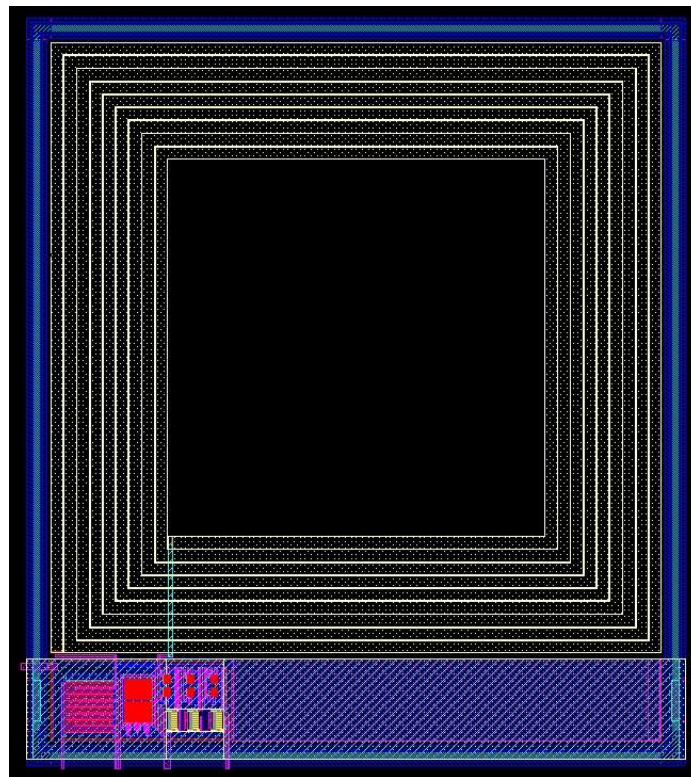
Fig. 32. Single-Channel MRI Front-End System Layout

The floorplan of the MRI system has four major components. The first two major components are two single-channel systems as seen as Figure 32. One channel is placed at the bottom left of the IC while the second channel is turned 180 degrees

and placed in the top right of the IC. In the top left of the IC, two preamplifiers are placed for the purpose of possible channels using off-chip coils. In the bottom right of the IC, two varactors and one preamplifier are placed for the purpose of test characterization. Once again, all unused area was filled in using polysilicon and all metals (1-4). Figure 33 shows the layout of the integrated circuit.

Fig. 33. MRI Front-End System Layout

The total area of the integrated circuit, including the padframe, is 4-mm by 4-mm. There are 44 functional pins to the circuit. The pin diagram for the circuit is shown in Figure 34. The respective pin descriptions of the IC pin diagram are listed in Table XIII on the next two pages.
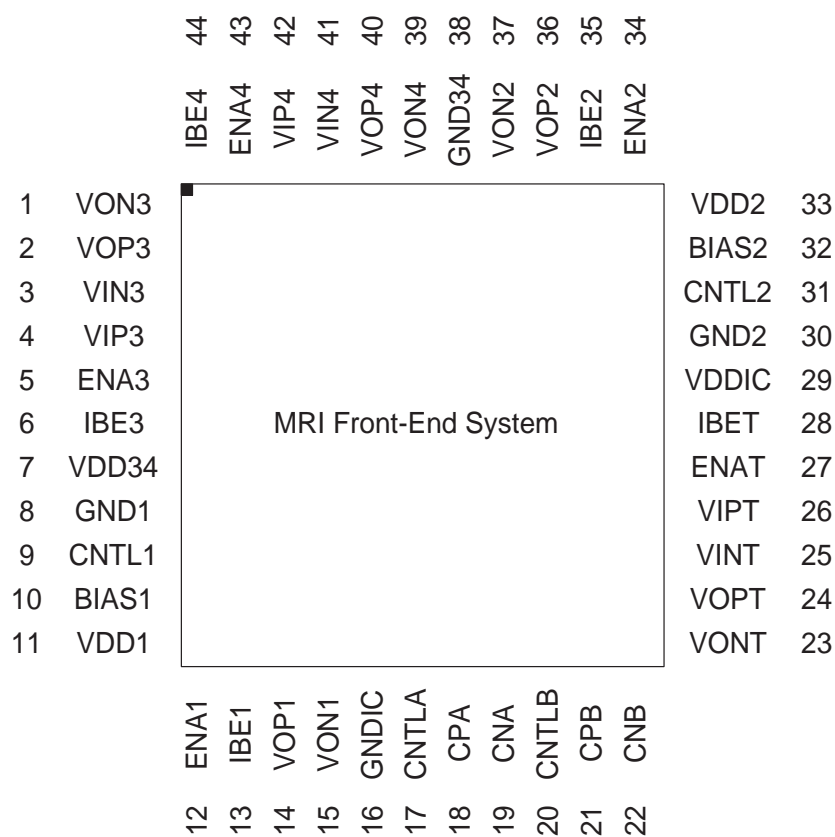
Fig. 34. MRI Front-End System Pin Diagram

Table XIII. MRI Front-End System Pin Description

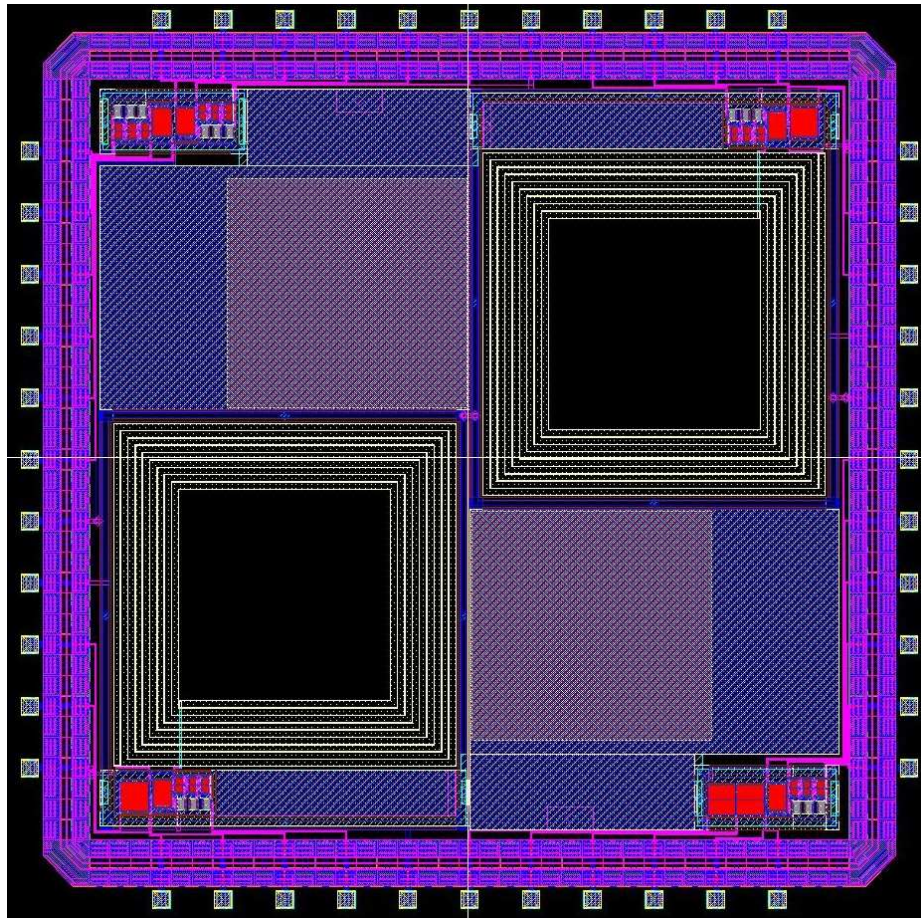| Pin #	Pin Name	Type	Description
1	VON3	Output	Preamplifier 3 Negative Voltage Output
2	VOP3	Output	Preamplifier 3 Positive Voltage Output
3	VIN3	Input	Preamplifier 3 Negative Voltage Input
4	VIP3	Input	Preamplifier 3 Positive Voltage Input
5	ENA3	Input	Preamplifier 3 Enable Voltage Input
6	IBE3	Input	Preamplifier 3 Bias Current Input
7	VDD34	Power	Preamplifier 3 & 4 Voltage Power Supply
8	GND1	Ground	Channel 1 Analog Ground
9	CNTL1	Input	Channel 1 Varactor Tuning Voltage Input
10	BIAS1	Input	Channel 1 DC Bias Voltage Input
11	VDD1	Power	Channel 1 Voltage Power Supply
12	ENA1	Input	Channel 1 Enable Voltage Input
13	IBE1	Input	Channel 1 Bias Current Input
14	VOP1	Output	Channel 1 Positive Voltage Output
15	VON1	Output	Channel 1 Negative Voltage Output
16	GNDIC	Ground	Integrated Circuit Analog Ground
17	CNTLA	Input	Test Varactor A Tuning Voltage Input
18	CPA	I/O	Test Varactor A Positive Node
19	CNA	I/O	Test Varactor A Negative Node
20	CNTLB	Input	Test Varactor B Tuning Voltage Input
21	CPB	I/O	Test Varactor B Positive Node
22	CNB	I/O	Test Varactor B Negative Node

Table XIII. Continued

Pin #	Pin Name	Type	Description
23	VONT	Output	Test Preamplifier Negative Voltage Output
24	VOPT	Output	Test Preamplifier Positive Voltage Output
25	VINT	Input	Test Preamplifier Negative Voltage Input
26	VIPT	Input	Test Preamplifier Positive Voltage Input
27	ENAT	Input	Test Preamplifier Enable Voltage Input
28	IBET	Input	Test Preamplifier Bias Current Input
29	VDDIC	Power	Integrated Circuit Voltage Power Supply
30	GND2	Ground	Channel 2 Analog Ground
31	CNTL2	Input	Channel 2 Varactor Tuning Voltage Input
32	BIAS2	Input	Channel 2 DC Bias Voltage Input
33	VDD2	Power	Channel 2 Voltage Power Supply
34	ENA2	Input	Channel 2 Enable Voltage Input
35	IBE2	Input	Channel 2 Bias Current Input
36	VOP2	Output	Channel 2 Positive Voltage Output
37	VON2	Output	Channel 2 Negative Voltage Output
38	GND34	Ground	Preamplifier 3 & 4 Analog Ground
39	VON4	Output	Preamplifier 4 Negative Output
40	VOP4	Output	Preamplifier 4 Positive Output
41	VIN4	Input	Preamplifier 4 Negative Input
42	VIP4	Input	Preamplifier 4 Positive Input
43	ENA4	Input	Preamplifier 4 Enable Voltage Input
44	IBE4	Input	Preamplifier 4 Bias Current Input

B.   Integrated Circuit Experimental Analysis

An important aspect of the circuit design is the experimental test phase. It is essential to have the integrated circuit receive and amplify a signal while suppressing the noise from other frequencies. The experimental procedure developed for the MRI system design shows that these test expectations have been met.

After layout of the circuit was completed, the design was sent to MOSIS for fabrication using the TSMC 0.35-μm CMOS Technology. After fabrication, the integrated circuit was packaged using the LQFP44A package type, which is an open-cavity, plastic casing with 44 pins. Once the design returned from fabrication, a microphotograph was taken of the integrated circuit die, which is seen in Figure 35.
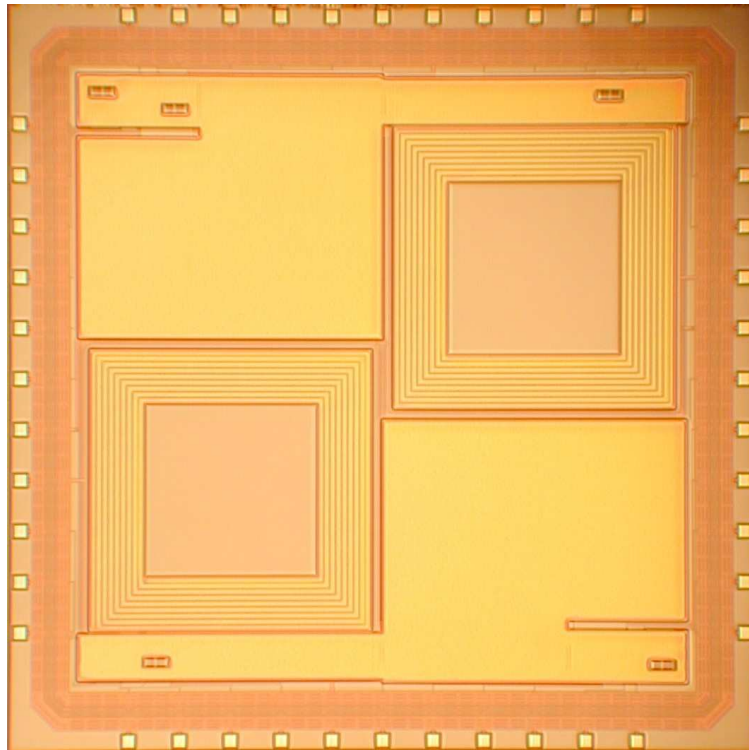

Fig. 35. MRI System Microphotograph

The circuit die size is 3.93 mm by 3.93 mm, which is equivalently equal to 15.445 mm². From the die photo, it is evident to see the two large microcoils, which will act as the detectors for the MRI system. Since metal density requirements are an issue for fabrication, most of the integrated circuit cannot be seen in the microphoto. Most of the circuitry and unused area of the die are covered by all metal layers and polysilicon in such a way to not disturb the system's functionality.

1.   Experimental Procedure

There are five experimental tests that will help determine the functionality of the MRI system. With the successful completion of each test, it will give positive and/or negative feedback for the next version of the MRI system prototype.

1. **DC Bias Characterization** A basic DC test at different nodes of the system to validate biasing is applied correctly.

2. **Varactor Characterization** Channel output voltage will be measured for different values of the varactor tuning voltage.

3. **MRI System Frequency Response** Channel output voltage response of the system will be analyzed with a common input voltage signal across the frequency spectrum.

4. **Co-Channel Interference Test** The output voltage response will be measured at different distances diagonally across the packaged integrated circuit to determine interference from the opposite channel.

5. **Signal-To-Noise Measurement** For a 200-MHz input signal, a ratio of the output signal and the system noise floor will be measured.

2. Experimental Setup

The diagram for the test setup of a single-channel of the MRI system is shown in Figure 36.
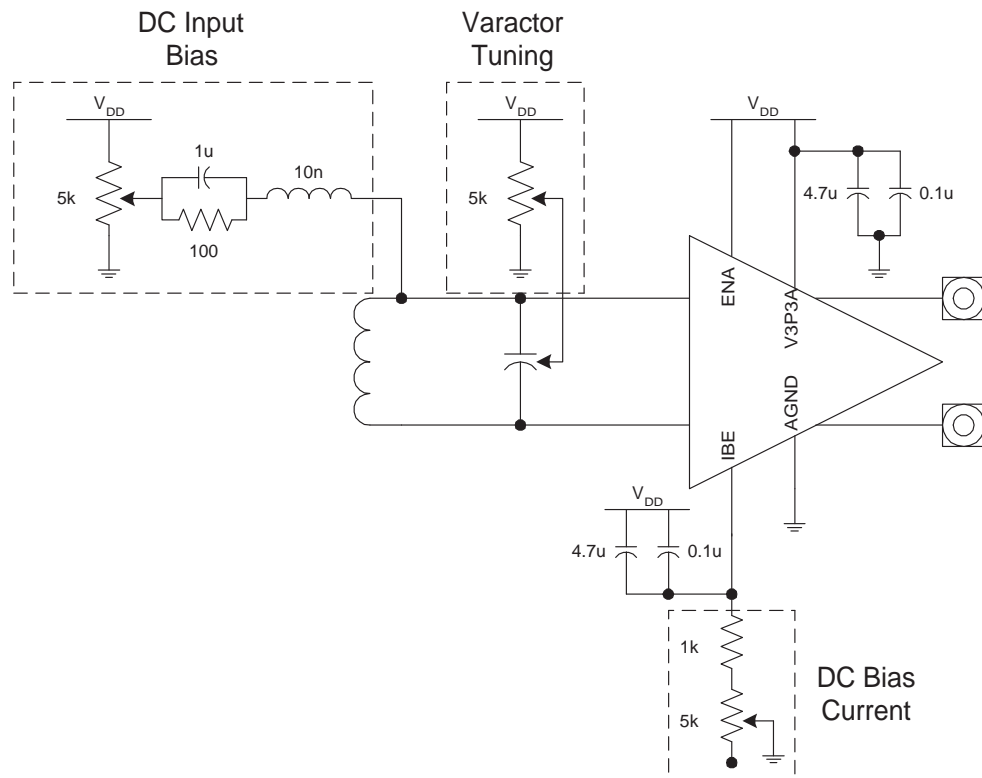
Fig. 36. Single-Channel MRI Front-End System Test Diagram

The capacitors that run from the power source to ground and the bias current source to the power source are needed to filter noise that may come from these two sources at higher frequencies. These capacitors are consisted of a 4.7-μF Tantulum capacitor in shunt with a 0.1-μF ceramic capacitor. The bias current source is accurately generated using a 1-kΩ resistor in series with a 5-kΩ variable resistor. The varactor tuning voltage is controlled by a 5-kΩ potentiometer acting as a voltage divider with the power source and ground. Another similar voltage divider is used to

control the DC bias of the input terminal of the preamplifier with the exception that it also contains a shunt combination of a 1-μF ceramic capacitor and 100-Ω resistor in series with 10-nH inductor. The purpose of this circuitry is to provide the necessary DC bias at the inputs while becoming an open circuit at higher frequencies. The entire printed circuit board (PCB) is shown in Figure 37 with the necessary extra circuitry for each channel.

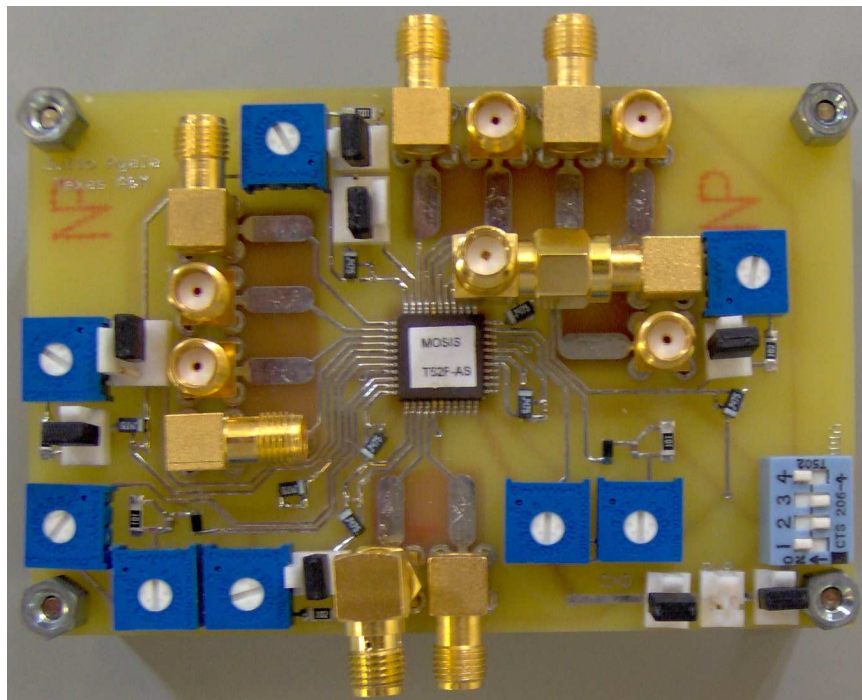Fig. 37. Printed Circuit Testboard

With the exception of the DC bias test, a signal must be generated and then transmitted to the microcoil on the integrated circuit. As seen in Figure 38, the signal generated will be coupled with an inductor to form a transformer with the microcoil on the chip. With some loss across the transformer, a signal can be detected on the microcoil and the system will function.
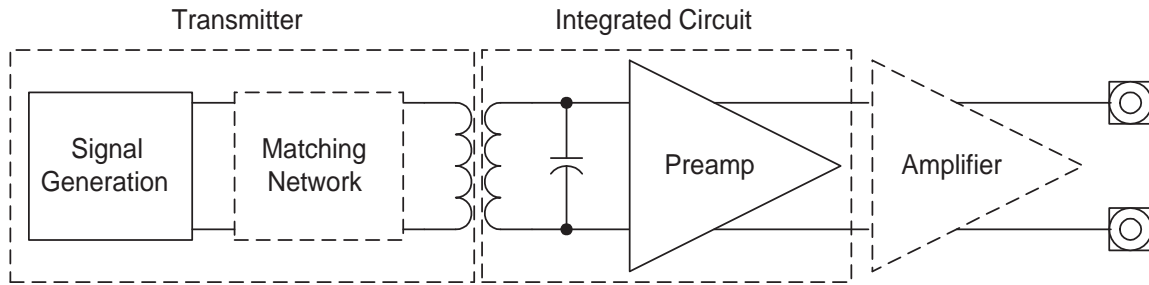
Fig. 38. Signal Generation Test Setup

The signal generation for these tests will either come from an oscillator or a network analyzer. In either case, the output impedance for these two instruments is 50-Ω. As seen in Figure 38, there will be a matching network to match the transmitter coil circuit to 50-Ω. Figure 39 shows the matching network for the signal generation test setup.
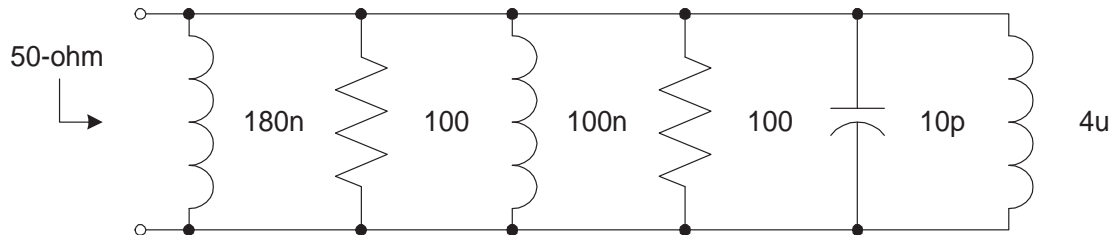
Fig. 39. 50-Ω Matching Network for Signal Transmitter

For the varactor characterization, co-channel interference test, and SNR measurement, a 200-MHz signal must be generated for the system. A Mini-Circuits ZX95-400 Voltage Controlled Oscillator (VCO) was used to generated a 2-V$_{pp}$, 200-MHz sinusoidal signal. Figure 40 shows the testboard for the VCO signal transmitter and Figure 41 shows the output signal seen across the transmitter coil circuit.
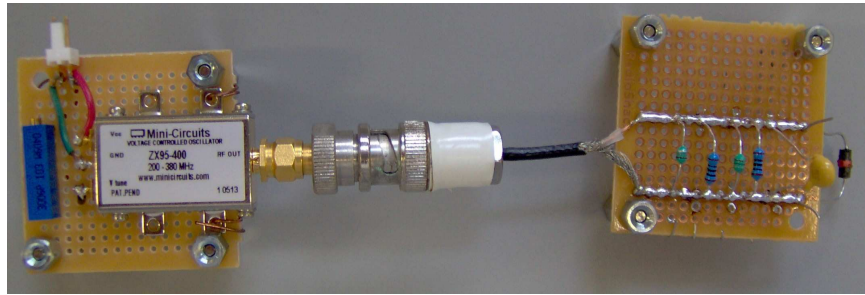
Fig. 40. VCO Signal Transmitter
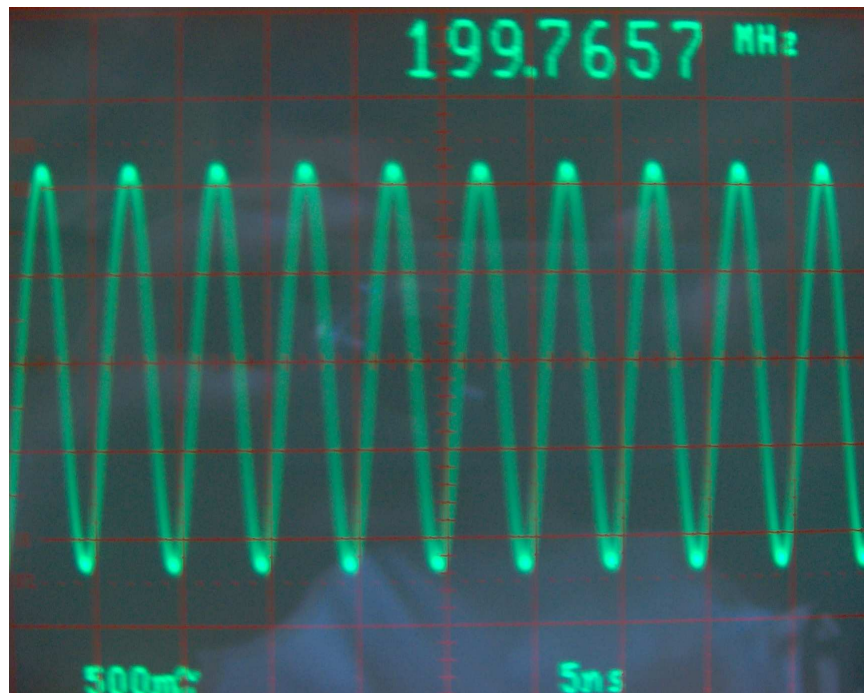
Fig. 41. Transmitter Signal

For the system frequency response, the VCO from Figure 40 is replaced with the RF output of the HP4395A Network Analyzer, which produces a constant 1-V signal across the frequency spectrum.

3. Experimental Results

The following sections will discuss and analyze the results of the five experimental tests conducted for the MRI front-end system.

a. DC Bias Characterization

The initial test on the system is the DC bias characterization. It is important that all biasing of the system is done correctly for proper functionality. This is done by supplying only a 3.3-V power source to the IC and adjusting all resistors to give the proper voltage for the input bias and bias current source. Table XIV shows the bias points for the most important points of the integrated circuit.

Table XIV. DC Bias Results

| DC Points	Simulation	Channel 1	Channel 2
$\mathbf{V}_{DD}$	3.30 V	3.31 V	3.31 V
Input DC Bias	1.65 V	1.65 V	1.65 V
Bias Current	1.95 mA	1.90 mA	1.91 mA
Output Positive Node	1.65 V	1.95 V	1.80 V
Output Negative Node	1.65 V	1.39 V	1.48 V

The DC bias points are closely approximated to the expected values for system with some small discrepancies at output voltage bias points. The output voltage bias points are a +/- 0.25 V difference than expected because of the POLY2 resistors. POLY2 resistors are known to fluctuate +/- 40% from the designed value after fabrication. In this case, the resistors have fluctuated no more than +/- 20% from their designed value.

b.   Varactor Characterization

The varactor characterization will show the performance of the system with a 200-MHz signal at different varactor tuning voltages. It is expected to see as the tuning voltage increases, the capacitance of the varactor will increase, thus changing the resonant frequency. As the varactor reaches its maximum tuning voltage, the capacitance value will be near a resonant frequency of 200-MHz with a maximum output voltage, as shown in Figure 42.
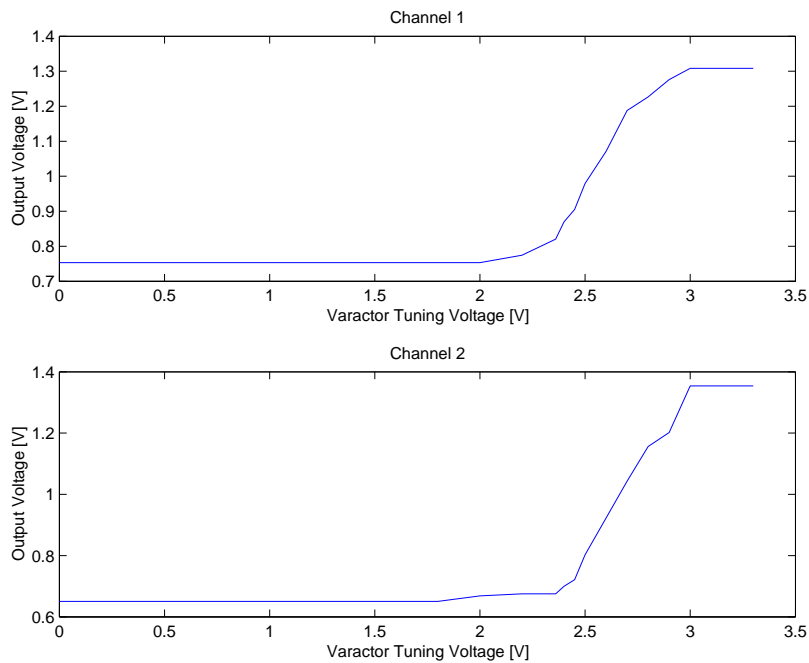
Fig. 42. Output Voltage vs. Varactor Tuning Voltage

Similar to what is seen in simulation, the tuning range of the varactor ranges from 2.4 V to 3.0 V. The actual capacitance at the maximum tuning voltage cannot be easily measured, therefore, the capacitance will be approximated using the experiment results from the system frequency response. Also, the range of capacitance of the varactor is limited, and it is difficult to see that as more capacitance is created, the

output voltage will begin to decrease. The reason for this is that an increase in capacitance will change the resonant frequency away from 200-MHz, thus decreasing the output voltage.

c.   MRI System Frequency Response

With a constant voltage across the frequency spectrum, the system will provide the characteristics of the microcoil such as the resonant frequency, the quality factor, and the capacitance of the varactor. Figure 43 shows the frequency response of Channels 1 & 2 for the MRI system.

Fig. 43. Output Voltage Frequency Spectrum

From the frequency response figure, the system quality factors can be determined by measuring the resonant frequency and the 3-dB cutoff frequencies. Using these frequencies and (4.3), the quality factor was calculated for each channel in Table XV.

Table XV. System Quality Factors

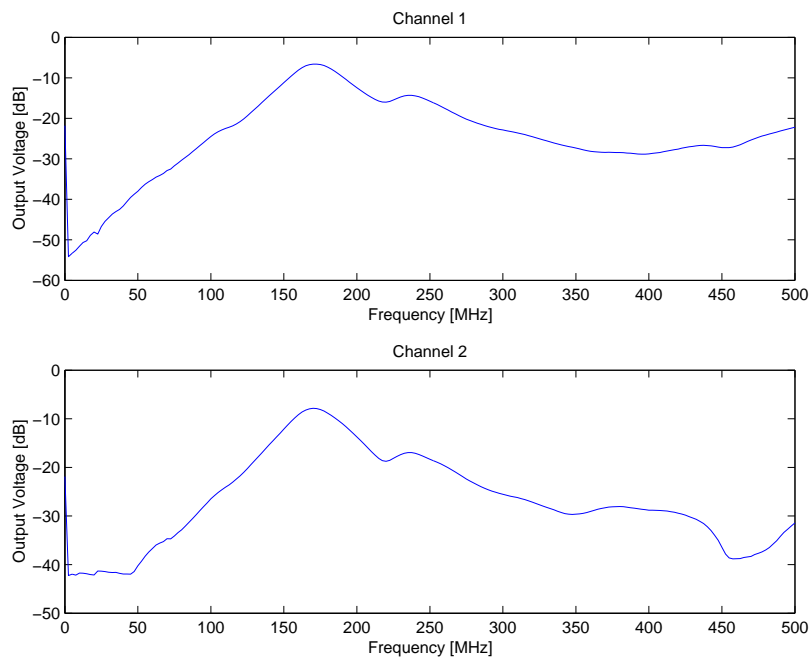| Nodes	Resonant Frequency	Lower 3-dB Frequency	Upper 3-dB Frequency	Quality Factor
Channel 1	170.0-MHz	155.0-MHz	187.5-MHz	5.2
Channel 2	170.0-MHz	155.0-MHz	187.5-MHz	5.2

As seen in Table XV, the resonant frequency is 170-MHz for each channel, which is 30-MHz below the designed value. Since the microcoil design is based by geometries, such as size, metal width, and metal spacing, the microcoil inductance value should be accurate to the designed value of 133-nH. Since the varactor is a transistor-based design, process variation and parasitics can greatly affect the capacitance. Therefore, the varactor capacitance has increased due to process variation and parasitics, thus, decreasing the resonant frequency. The microcoil inductance is assumed to be 133-nH +/- 15%, the varactor capacitance will be calculated using (2.4), and the series resistance will be calculated using (2.5). Tables XVI, XVII, and XVIII show the varactor capacitance and series resistance at different microcoil inductances.

Table XVI. Microcoil Characteristics for Nominal Microcoil Inductance

Nodes	Q	Inductance	Capacitance	Resistance
Channel 1	5.2	133.4 nH	6.6 pF	27.2 Ω
Channel 2	5.2	133.4 nH	6.6 pF	27.2 Ω

After reviewing the results from the frequency response, the inductance, the series resistance, and the quality factor are comparable to the design values. The capacitance has increased due to process variation and parasitics, thus, decreasing the resonant frequency of the system.

Table XVII. Microcoil Characteristics for -15% of Nominal Microcoil Inductance

Nodes	Q	Inductance	Capacitance	Resistance
Channel 1	5.2	113.4 nH	7.7 pF	23.2 Ω
Channel 2	5.2	113.4 nH	7.7 pF	23.2 Ω

Table XVIII. Microcoil Characteristics for +15% of Nominal Microcoil Inductance

Nodes	Q	Inductance	Capacitance	Resistance
Channel 1	5.2	153.4 nH	5.7 pF	31.3 Ω
Channel 2	5.2	153.4 nH	5.7 pF	31.3 Ω

d.   Co-Channel Interference Test

An important experimental test for this system is the co-channel interference. There is a need to figure how well these microcoils detect a signal while avoiding the detection of signals on the opposite channel. In order to test for co-channel interference, a movable probe station (Figure 44) was used to mount the 200-MHz signal while keeping the MRI system testboard stationary.
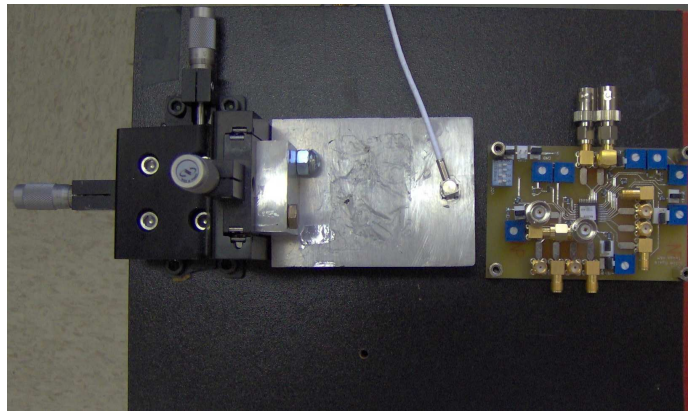
Fig. 44. Channel Interference Probe Station

The metal platform on the station is approximately 4 in by 3 in. The transmitter with the VCO as the signal source, as seen in Figure 40, was mounted firmly on the metal platform with the large inductor hanging down across the integrated circuit on the stationary testboard. Again, the transmitter signal generated is a 2-V_{pp}, 200-MHz sinusoid from the VCO. The probe station allows the movement of the signal in steps of 0.5 millimeters diagonally across the integrated circuit, as seen in Figure 45. The signal source was approximately 1 mm above the circuit on the testboard. The total distance diagonally across the circuit is 14 mm, while the center-to-center spacing between the two microcoils is 2 mm.
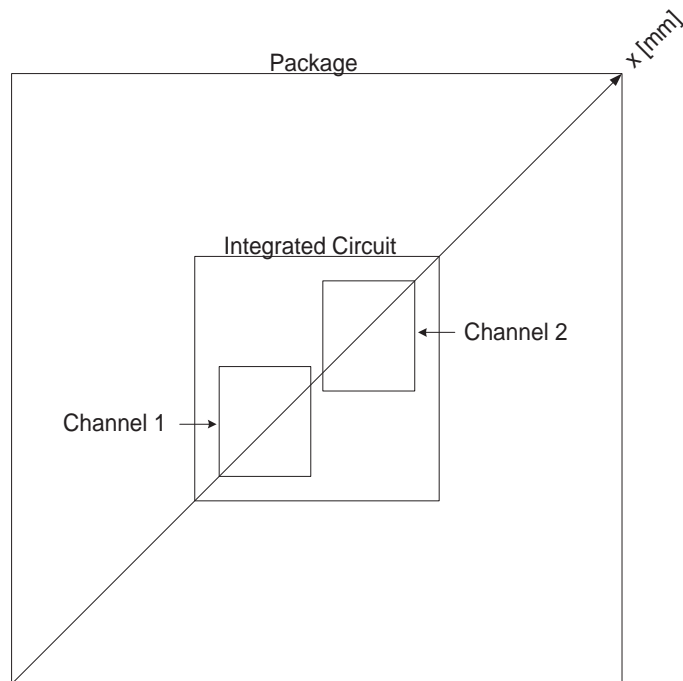
Fig. 45. Channel Interference Diagram

As the signal moves diagonally across the circuit, the output voltage of each channel is measured at different 0.5 mm intervals. It is expected to see that the maximum peak signal at each channel will occur at different distances from one

another. With a large the separation of maximum signals between the two channels, the less interference each channel will incur on each other.
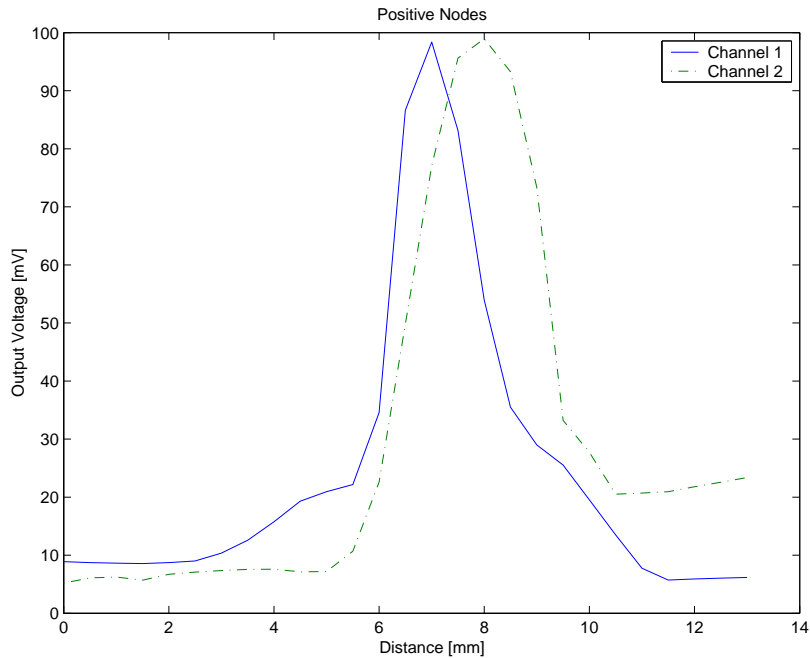
Fig. 46. Output Voltage for Various Distances

Figure 46 shows the results of the co-channel interference. This shows the maximum peak output signal detected at each channel is separated by approximately 1 millimeter. Since the center-to-center spacing of the microcoils is 2 mm apart, the signal separation could have been at the same distance. It is believed that the microcoil gets stronger when it becomes closer to the adjacent microcoil because a small portion of the signal gets fed into it, which shifts the peak signal of each channel a closer distance together. Some modifications to layout that can be made to increase the separation of the peak signals may be to add more guard rings around each separate channel and managing to place the microcoils further apart in the floorplan.

e. Signal-to-Noise Measurement

The signal-to-noise (SNR) measurement provides information as comparison to previous studies of an MRI front-end system. The best SNR measurement for a similar type of front-end system is provided by Stocker, who measured a SNR of 25 [21]. The SNR was calculated by the ratio of the maximum signal power [dB], $V_{o,max}$ seen in the frequency spectrum to the noise spectrum [dB/Hz], V_{noise} multiply with the bandwidth (5-MHz). Since the maximum power signal and the noise spectrum are in terms of decibels (dB), the logarithmic properties for multiplication and division applies to the SNR equation, as seen in (5.1).

$$SNR[dB] = V_{o,max} - (V_{noise} + 10 \cdot log10\,(5E+06)) \tag{5.1}$$
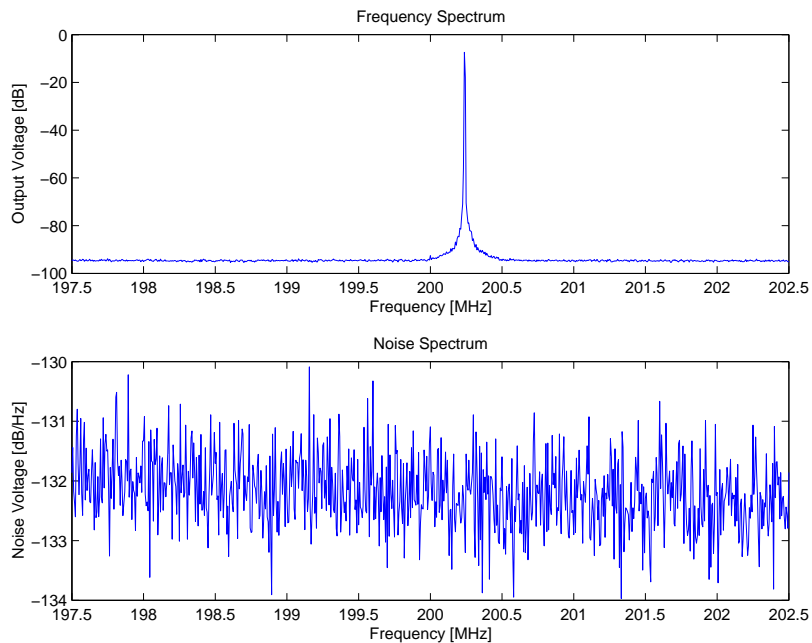
Fig. 47. Output Voltage Frequency and Noise Spectrum for Channel 1

Figures 47 and 48 show the frequency and noise spectrum of Channel 1 and 2 when a 200-MHz signal is applied to the system. Using the data collected for each channel
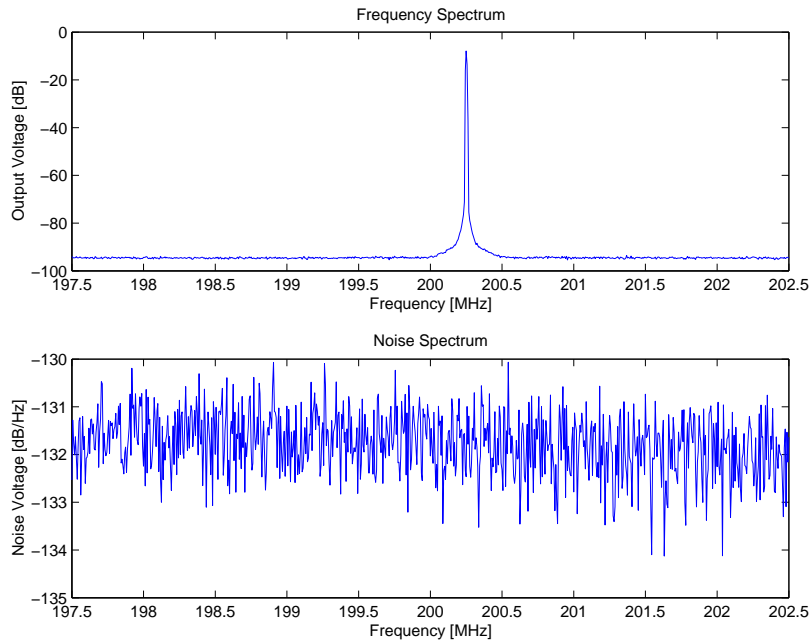
Fig. 48. Output Voltage Frequency and Noise Spectrum for Channel 2

and MATLAB, a basic SNR measurement for each channel is shown in Table XIX.

Table XIX. SNR Results

Nodes	SNR
Channel 1	57.77 dB
Channel 2	56.86 dB

The SNR results are larger in comparison with the results of Stocker due to the input signal of the front-end system. Since the output signal of system was approximately -10 dB (approximately a few hundred millivolts) for each channel and the preamplifier gain was approximately 40 dB, the input signal of the system is approximately a few millivolts. The input signal will be a few microvolts for most standard MRI systems. With such a small input signal, the output signal will also be small, thus, the SNR measurements will decrease and become comparable to [21].

CHAPTER VI

CONCLUSION

With the growing trend of research in nuclear magnetic resonance, there has been significant interest in designing integrated sensors for magnetic resonance imaging. In continuing this trend, the purpose of this project was to research and design a prototype two-channel, front-end integrated sensor for a MRI system with an on-chip microcoil. The project has succeeded in producing good functionality for a multiple-channel sensor. The sensor met expectations compared to similar one-channel systems through experiments in channel separation and good signal-to-noise ratios.

A. Future Work

Since the integrated circuit was a first prototype, there is always room for improvement and future work. Although testing the IC for functionality is important, a test of the front-end system inside the MRI magnetic core should be considered in the next version of the prototype. A complete digital microcoil system should be considered, which includes the narrow-band bandpass filter and mixer to down-convert the 200-MHz signal for an analog-to-digital converter. New architectures for the microcoil and preamplifier can be considered to better optimize the system such as quality factor and low noise properties. Also, a multiple-channel digital coil array with a multiplexer for digital signal processing is the most advanced future project that will be considered. Ultimately, this research should move toward creating a 32 to 64-channel array system on an IC to compare with the state-of-art, non-IC MRI front-end systems.

REFERENCES

[1] J. Hornak, "Basics of NMR," New York: Rochester Institute of Technology, Available: http://www.cis.rit.edu/htbooks/nmr/bnmr.htm, 1999.

[2] Z. Liang and P. Lauterbur, *Prinicples of Magnetic Resonance Imaging.* New York: The Institute of Electrical and Electronics Engineers, Inc., 2000.

[3] S. Wright, *Introduction to Biomedical Engineering.* New York: Academic Press, 1999, ch. 16, pp. 783–841.

[4] S. Wright, M. McDougall, and D. Brown, "Single Echo Acquistion of MR Images Using RF Coil Arrays," in *Proceedings of the Second Joint EMBS/BMES Conference*, Houston, October 2002, pp. 1181–1182.

[5] L. Berry, L. Renaud, P. Kleimann, P. Morin, M. Armenean, and H. Saint-Jalmes, "Implantable Solenoidal Microcoil for Nuclear Magnetic Resonance Spectroscopy," in *First Annual International IEEE-EMBS Special Topic Conference on Microtechnologies in Medicine and Biology*, Lyon, France, October 2000, pp. 171–174.

[6] J. Stocker, T. Peck, A. Webb, M. Feng, and R. Magin, "Nanoliter Volume, High-Resolution Nuclear Magnetic Resonance Microspectroscopy Using a 60-um Planar Microcoil," *IEEE Transactions on Biomedical Engineering*, vol. 44, pp. 1122–1127, November 1997.

[7] B. Razavi, *RF Microelectronics.* Upper Saddle River, NJ: Prentice Hall, 1998.

[8] T. Mareci, "Basic Design Principles of Magnetic Resonance Coils," unpublished course notes, Gainesville: University of Florida, 2003.

[9] A. Niknejad, "Modeling of Passive Elements with ASITIC," in *2002 IEEE Radio Frequency Integrated Circuits Symposium*, Seattle, June 2002, pp. 303–306.

[10] A. Niknejad and R. Meyer, "Analysis, Design, and Optimization of Spiral Inductors and Transformers for Si RF IC's," *IEEE Journal of Solid-State Circuits*, vol. 33, pp. 1470–1481, October 1998.

[11] Y. Chen, D. Heo, J. Laskar, and T. Anderson, "Investigation of Q Enhancement for Inductors Processed in BiCMOS Technology," in *1999 IEEE Radio and Wireless Conference*, Denver, August 1999, pp. 263–266.

[12] D. Shaeffer and T. Lee, "A 1.5-V, 1.5-GHz CMOS Low Noise Amplifier," *IEEE Journal of Solid-State Circuits*, vol. 32, pp. 745–759, May 1997.

[13] A. Karanicolas, "A 2.7-V 900-MHz CMOS LNA and Mixer," *IEEE Journal of Solid-State Circuits*, vol. 31, pp. 1939–1944, December 1996.

[14] T. Nguyen and S. Lee, "A 5.2 Ghz, 1.7 dB NF Low Noise Amplifier for Wireless LAN Based on 0.18 um CMOS Technology," in *2002 3rd International Conference on Microwave and Millimeter Wave Technology Proceedings*, Beijing, August 2002, pp. 251–254.

[15] G. Gonzalez, *Microwave Transistor Amplifiers: Analysis and Design*. Upper Saddle River, NJ: Prentice Hall, 1997.

[16] B. Razavi, *Design of Analog CMOS Integrated Circuits*. New York: McGraw Hill, 2001.

[17] R. Schaumenn and M. V. Valkenburg, *Design of Analog Filters*. New York: Oxford University Press, 2001.

[18] T. Sumesaglam, "Automatic Tuning of Continuous-Time Filters," Ph.D. dissertation, College Station: Texas A&M University, 2004.

[19] S. Franco, *Design with Operational Amplfiers and Analog Integrated Circuits*, 3rd ed. St. Louis: McGraw Hill, 2002.

[20] D. Johns and K. Martin, *Analog Integrated Circuit Design*. New York: John Wiley & Sons, Inc., 1997.

[21] J. Stocker, T. Peck, S. Franke, J. Kruse, M. Feng, and R. Magin, "Development of an Integrated Detector for NMR Microscopy," in *17th Annual International Conference of the IEEE Engineering in Medicine and Biology Society*, Montreal, September 1995, pp. 843–844.

APPENDIX A

ASITIC TECHNOLOGY FILE


```
; TSMC 0.35um CMOS technology file for ASITIC
<chip>
        chipx = 512      ; dimensions of the chip in x direction
        chipy = 515      ; dimensions of the chip in y direction
        fftx  = 256      ; x-fft size (must be a power of 2)
        ffty  = 256      ; y-fft size
        TechFile = tsmc35.tek
        TechPath = .
        freq  = 1        ; frequency of operation
        eddylayer = 0
        eddylayer = 1

<layer> 0                ; p(-) bulk layer
        rho = .1         ; ohm-cm
        t   = 400        ; microns
        eps = 11.9

<layer> 1                ; Oxide Layer
        rho = 1e10
        t   = 8
        eps = 3.9

<metal> 0
        layer = 1        ; in oxide layer
        rsh   = 7.3      ; sheet resistance3,milli-ohms per square
        t     = 0.275    ; thickness
        d     = 0.29     ; distance from bottom of layer
        name  = p1
        color = red

<metal> 1
        layer = 1        ; in oxide layer
        rsh   = 80       ; sheet resistance3
        t     = 0.665    ; thickness
        d     = 1.21     ; distance from bottom of layer
        name  = m1
        color = yellow

<metal> 2
        layer = 1
        rsh   = 80
        t     = 0.64
        d     = 2.875
```

```
        name  = m2
        color = LightSkyBlue1

<metal> 3
        layer = 1
        rsh   = 70
        t     = 0.64
        d     =   4.515
        name  = m3
        color = medium purple

<metal> 4
        layer = 1
        rsh   = 40
        t     = 0.925
        d     =   6.155
        name  = m4
        color = light green

<via> 0                        ; metal 1 to metal 2
        top       = 2
        bottom    = 1
        r         = 1.53
        width     = .4
        space     = .6
        overplot1 = .2  ; to metal 1
        overplot2 = .2  ; to metal 2
        name      = via1
        color     = purple

<via> 1                        ; metal 2 to metal 3
        top       = 3
        bottom    = 2
        r         = 1.46
        width     = .4
        space     = .6
        overplot1 = .2  ; to metal 2
        overplot2 = .2  ; to metal 3
        name      = via2
        color     = cyan1

<via> 2                        ; metal 3 to metal 4
        top       = 4
        bottom    = 3
        r         = 1.36
        width     = .4
        space     = 1.2
        overplot1 = .2
        overplot2 = .4
        name      = via3
        color     = red
```

APPENDIX B

EXPERIMENTAL ANALYSIS MATLAB CODE


```matlab
% Julio Ayala
% File: Vout_Vdc.m
% Varactor DC Bias Analysis

% Requires Vout_Vdc_DATA.txt
% Contains experimental data

[vdc v1p v1n v2p v2n] =
 textread('Vout_Vdc_DATA.txt','%f %f %f %f %f');

figure(1)
subplot(2,1,1),plot(vdc,((v1p+v1n)/(2*sqrt(2))))
title('Channel 1');
xlabel('Varactor Tuning Voltage [V]');
ylabel('Output Voltage [V]');
subplot(2,1,2),plot(vdc,((v2p+v2n)/(2*sqrt(2))))
title('Channel 2');
xlabel('Varactor Tuning Voltage [V]');
ylabel('Output Voltage [V]');
print -dpsc vout_vdc

% Julio Ayala
% File: Vout_Freq.m
% Frequency Response Analysis

% Requires Vout_Freq_DATA.txt
% Contains experimental data

close all; clear all;
[f v1p v1n v2p v2n] =
 textread('Vout_Freq_DATA.txt','%f %f %f %f %f');

v1 = 20*log10(10.^(v1p/20) + 10.^(v1n/20));
v2 = 20*log10(10.^(v2p/20) + 10.^(v2n/20));

figure(1)
subplot(2,1,1),plot(f/1e6,v1)
title('Channel 1');
xlabel('Frequency [MHz]');
ylabel('Output Voltage [dB]');
subplot(2,1,2),plot(f/1e6,v2)
title('Channel 2');
xlabel('Frequency [MHz]');
```

```
ylabel('Output Voltage [dB]');
print -dpsc vout_freq

out = fopen('Vout_Freq.TXT','w');

L = 133.4e-9;        % Microcoil Approximate Inductance

% Channel 1
[V,I] = max(v1);
rf = f(I);
index = I;
while v1(I) > V - 3,
    f1 = f(I);
    I = I - 1;
end
I = index;
while v1(I) > V - 3,
    f2 = f(I);
    I = I + 1;
end
Q = rf / (f2 - f1);
cap = 1 / ((2 * pi * rf)^2 * L);
fprintf(out,'Channel 1:    fo = %3.1f MHz    f1 = %3.1f MHz
    f2 = %3.1f MHz    Q = %3.1f    C = %3.1f pF    L = %3.1f nH
    R = %3.1f\n',rf/1e6,f1/1e6,f2/1e6,Q,cap/1e-12,L/1e-9,2*pi*rf*L/Q);

% Channel 2
[V,I] = max(v2);
rf = f(I);
index = I;
while v2(I) > V - 3,
    f1 = f(I);
    I = I - 1;
end
I = index;
while v2(I) > V - 3,
    f2 = f(I);
    I = I + 1;
end
Q = rf / (f2 - f1);
cap = 1 / ((2 * pi * rf)^2 * L);
fprintf(out,'Channel 2:    fo = %3.1f MHz    f1 = %3.1f MHz
    f2 = %3.1f MHz    Q = %3.1f    C = %3.1f pF    L = %3.1f nH
    R = %3.1f\n',rf/1e6,f1/1e6,f2/1e6,Q,cap/1e-12,L/1e-9,2*pi*rf*L/Q);

fclose(out);

% Julio Ayala
% File: Vout_Distance.m
% Co-Channel Interference Plot
```

```
% Requires Vout_Distance_DATA.txt
% Contains experimental data

close all; clear all;
[x v1p v1n v2p v2n] =
 textread('Vout_Distance_DATA.txt','%f %f %f %f %f');

figure(1)
plot(x,(10.^(v1p/20)+10.^(v1n/20))/1e-3,
     x,(10.^(v2p/20)+10.^(v2n/20))/1e-3,'-.')
title('Positive Nodes');
xlabel('Distance [mm]');
ylabel('Output Voltage [mV]');
legend('Channel 1','Channel 2');
print -dpsc vout_distance

% Julio Ayala
% File: Vout_Spectrum.m
% Frequency Response Analysis

% Requires Vout_Freq_DATA.txt
% Contains experimental data

clear all; close all;

[f,OSP,ONP,OSN,ONN,TSP,TNP,TSN,TNN] =
 textread('Vout_Spectrum_DATA.txt','%f %f %f %f %f %f %f %f %f');

OS = 20*log10(10.^(OSP/20)+10.^(OSN/20))
ON = 20*log10(10.^(ONP/20)+10.^(ONN/20))
TS = 20*log10(10.^(TSP/20)+10.^(TSN/20))
TN = 20*log10(10.^(TNP/20)+10.^(TNN/20))

% Channel 1
figure(1)
subplot(2,1,1),plot(f/1e6,OS)
title('Frequency Spectrum');
xlabel('Frequency [MHz]');
ylabel('Output Voltage [dB]');
subplot(2,1,2),plot(f/1e6,ON)
title('Noise Spectrum');
xlabel('Frequency [MHz]');
ylabel('Noise Voltage [dB/Hz]');
print -dpsc vout_spectrum_ch1

% Channel 2
figure(2)
subplot(2,1,1),plot(f/1e6,TS)
title('Frequency Spectrum');
xlabel('Frequency [MHz]');
ylabel('Output Voltage [dB]');
```

```
subplot(2,1,2),plot(f/1e6,TN)
title('Noise Spectrum');
xlabel('Frequency [MHz]');
ylabel('Noise Voltage [dB/Hz]');
print -dpsc vout_spectrum_ch2

out = fopen('Vout_Spectrum.TXT','w');

% SNR Measurements
SNR1_1 = SNR1(f,OS);
SNR1_2 = SNR1(f,TS);

SNR2_1 = SNR2(f,OS,ON);
SNR2_2 = SNR2(f,TS,TN);

fprintf(out,'Channel 1:
  SNR1 = %4.2f dB   SNR2 = %4.2f dB\n',SNR1_1,SNR2_1);
fprintf(out,'Channel 2:
  SNR1 = %4.2f dB   SNR2 = %4.2f dB\n',SNR1_2,SNR2_2);

fclose(out);

% Julio Ayala
% File: SNR1.m
% SNR Method 1 Function

function [SNR] = SNR1(f,data)

k = length(f);
df = f(2) - f(1);
Esig = 0;
Enoise = 0;

for m = 1 : 1 : k
    if data(m) > -80
        sig = 10^(data(m) / 20);
        noise = 0;
    else
        sig = 0;
        noise = 10^(data(m) / 20);
    end
    Esig = Esig + sig * df;
    Enoise = Enoise + noise * df;

end

SNR = 20 * log10(Esig/Enoise);


% Julio Ayala
% File: SNR2.m
```

```
% SNR Method 2 Function

function [SNR] = SNR2(f,signal,noise)

k = length(f);
df = f(2) - f(1);
Esig = 10^(max(signal) / 10);
Enoise = 0;

for m = 1 : 1 : k - 1
    Enoise = Enoise + 10^(noise(m) / 10) * df;
end

SNR = 10 * log10(Esig/Enoise);
```

VITA

Julio Enrique Ayala II was born in San Antonio, Texas. He received his Bachelor of Science degree in Computer Engineering - Electrical Engineering Track from Texas A&M Unviersity in December 2001. He worked at Advanced Mirco Devices as a chipset verification engineer from January 2002 to August 2002. He joined the graduate program in electrical engineering at Texas A&M University in August 2002. He worked as a co-op in the Storage Products Group (Servo) at Texas Instruments in the summer of 2004. He received his Master of Science degree in Electrical Engineering in December 2005. His research interests are in the area of analog and mixed signal integrated circuit design. As of August 2005, he is employed as a integrated circuit design engineer at Texas Instruments in Dallas. He can be reached via his email address, jeayala@gmail.com, or his permanent address at 1443 Peterson Avenue, San Antonio, TX 78224.